AGU PUBLICATIONS

JGR

Journal of Geophysical Research: Planets

RESEARCH ARTICLE
10.1002/2014JE004669

This article is a companion to *Lee et al.* [2014] doi:10.1002/2013JE004552.

Key Points:
- Solar cycle and seasonal variability of hot C corona is simulated in 3-D
- Our simulation considered PD of CO and DR of CO^+ as main sources
- The estimated escape rates range from 5.28 to 55.1E23 s^{-1}

Correspondence to:
Y. Lee,
yunilee@umich.edu

Citation:
Lee, Y., M. R. Combi, V. Tenishev, and S. W. Bougher (2014), Hot carbon corona in Mars' upper thermosphere and exosphere: 2. Solar cycle and seasonal variability, *J. Geophys. Res. Planets*, *119*, 2487–2509, doi:10.1002/2014JE004669.

Received 19 MAY 2014
Accepted 4 NOV 2014
Accepted article online 10 NOV 2014
Published online 5 DEC 2014

Hot carbon corona in Mars' upper thermosphere and exosphere: 2. Solar cycle and seasonal variability

Yuni Lee[1], Michael R. Combi[1], Valeriy Tenishev[1], and Stephen W. Bougher[1]

[1]Department of Atmospheric, Oceanic and Space Sciences, University of Michigan, Ann Arbor, Michigan, USA

Abstract This work presents the variability over seasons (i.e., orbital position) and solar cycle of the Martian upper atmosphere and hot carbon corona. We investigate the production and distribution of energetic carbon atoms and the impacts on the total global hot carbon loss from dominant photochemical processes at five different cases: AL (aphelion and low solar activity), EL (equinox and low solar activity), EH (equinox and high solar activity), PL (perihelion and low solar activity), and PH (perihelion and high solar activity). We compare our results with previously published results but only on the limited cases due to the dearth of studies on solar EUV flux and seasonal variabilities. Photodissociation of CO and dissociative recombination of CO^+ are generally regarded as the two most important source reactions for the production of hot atomic carbon. Of these two, photodissociation of CO is found to be the dominant source in all cases considered. To describe self-consistently the exosphere and the upper thermosphere, a 3-D kinetic particle simulator, the Adaptive Mesh Particle Simulator, and the 3-D Mars Thermosphere General Circulation Model are one-way coupled. The basic description of this hot carbon calculation can be found in the companion paper to this one. The spatial distributions and profiles of density and temperature and atmospheric loss rates are discussed for the cases considered. Finally, our computed global escape rate of hot carbon ranges from $5.28 \times 10^{23}\ s^{-1}$ (AL) to $55.1 \times 10^{23}\ s^{-1}$ (PL).

1. Introduction

The inventory of water and CO_2 on Mars is constrained primarily by the escape of ions and neutrals that contain H, C, and O elements. In particular, the escape of heavy neutral atoms is induced by nonthermal mechanisms in the Martian atmosphere with speeds above the escape speed. A newly produced hot carbon atom escapes to space when it reaches the collisionless region with the energy of about 1.48 eV. Otherwise, it travels until being thermalized by the interaction with the ambient cold neutral atmosphere, or moves along its ballistic trajectory in the exosphere with energy below the escape energy, eventually falling back to the thermosphere.

The hot carbon corona has been observed at Venus by the UV spectrometer aboard the Pioneer Venus Orbiter [e.g., *Paxton*, 1985]. However, there has not been any observation of the Martian hot carbon corona. As a first mission to devote to explore the upper atmosphere of Mars, the new Mars scout mission, Mars Atmosphere and Volatile EvolutioN (MAVEN), has recently arrived at Mars and is expected to expand our knowledge on the detailed structure of the Martian hot corona. Our understanding of the Martian atmospheric loss has been vastly improved by thorough numerical modeling efforts in both current and evolutionary aspects. However, most of the works have focused on the hot oxygen corona [e.g., *Fox and Hać*, 2009; *Fox*, 1997a; *Kim et al.*, 1998; *Hodges*, 2000; *Cipriani et al.*, 2007; *Valeille et al.*, 2009a, 2009b, 2010a, 2010b; *Yagi et al.*, 2012]; only a few numerical approaches have been carried out for the hot carbon corona investigation [*Cipriani et al.*, 2007; *Fox*, 2004; *Fox and Bakalian*, 2001; *Fox and Hać*, 1999; *Nagy et al.*, 2001].

These previous studies have suggested various nonthermal mechanisms that can induce the escape of C atoms. The most important nonthermal source reaction for the production of hot C is assumed to be photodissociation of CO [e.g., *Fox*, 2004; *Fox and Bakalian*, 2001; *Nagy et al.*, 2001]. Other potential source mechanisms can be, for example, photoelectron impact dissociation of CO, dissociative recombination of CO_2^+, and photoelectron impact dissociation of CO_2 [*McElroy et al.*, 1977; *Fox and Bakalian*, 2001]. Among these potential source mechanisms, dissociative recombination of CO^+ has been suggested as another nonnegligible source that must be considered in the computation of the total escape rate of hot C [e.g., *Fox*,

2004; *Fox and Hać*, 1999; *Fox and Bakalian*, 2001; *Nagy et al*., 2001]. As many of the previous hot C studies [*Cipriani et al*., 2007; *Fox and Bakalian*, 2001; *Fox and Hać*, 1999; *Nagy et al*., 2001] suggested, this study considers photodissociation of CO and dissociative recombination of CO^+ only as the main sources of hot C on Mars.

C loss also occurs by the escape of C-containing ions and sputtering, induced by the solar wind interaction with the hot C corona. Neutral species in the hot coronae can be ionized by photons, electron impacts or charge exchange reactions in the upper atmosphere [e.g., *Luhmann et al*., 1992; *Jakosky et al*., 1994; *Johnson*, 1994; *Leblanc and Johnson*, 2001]. First observed by the PHOBOS-2 spacecraft [*Lundin et al*., 1990; *Verigin et al*., 1991], these heavy ions newly produced from the interaction of the solar wind with the exosphere can (1) be picked up by the convection fields of the solar wind plasma and directly lost to space or (2) reimpact the atmosphere and initiate the momentum transfer events, causing neutrals to escape from the hot coronae, known as sputtering [*Luhmann and Kozyra*, 1991]. The loss of C atoms via ion escape and sputtering is comparable to that by the aforementioned photochemical mechanisms. The physics of the Mars-solar wind interaction has been successfully simulated and addressed by various models. Recent model studies have provided, for example, the upper limits to the outflow of heavy ions [*Fox*, 1997b] and realistic descriptions of pickup O^+ ion distributions around Mars using multispecies 3-D MHD models [*Liu et al*., 1999, 2001; *Ma et al*., 2004; *Ma and Nagy*, 2007; *Fang et al*., 2008] and multifluid 3-D MHD model [*Dong et al*., 2014]. *Fang et al*. [2013] have carried out case studies of pickup ion precipitation under various extreme solar wind conditions, and *Curry et al*. [2013] have extensively assessed the different source mechanisms of pickup ions. In the investigation of nonthermal atmospheric loss, these studies can serve as a significant tool for understanding the sputtering of hot O and hot C.

The Martian hot corona is formed from the upper thermosphere and ionosphere where important mechanisms and dynamics, such as production and loss of the thermospheric, ionospheric, and hot species, take place. In order to model the Martian upper atmosphere self-consistently, we used a 3-D global kinetic model to describe the physics of particle interaction and escape and a 3-D thermosphere/ionosphere model to provide a description resolving the inherent limitations of the past 1-D and 2-D models. The model details, basic hot C corona structures, and resulting effects and advantages of a 3-D atmosphere input have discussed in the work of *Lee et al*. [2014, hereafter referred to as Paper I] to emphasize the need of inclusion of the thermosphere dynamics. Paper I considered a fixed orbital position and solar activity condition, the equinox and low solar activity case (EL), for the purpose of the rigorous investigation of the mechanisms in the upper atmosphere.

In this study, the same approaches are used to study the variabilities of the hot C corona and the atmospheric loss for different solar activity and orbital positions (seasons: aphelion/equinox/perihelion). The Martian upper atmosphere and hot C corona are extensively described by a full 3-D study of the exosphere presented here. The 3-D Mars Thermosphere General Circulation Model (MTGCM) [e.g., *Bougher et al*., 2006, 2009] provides all necessary thermospheric/ionospheric parameters as a suite of inputs to our 3-D kinetic particle simulator [*Tenishev et al*., 2013] with the Martian exosphere code implemented. The latter is called Mars-Adaptive Mesh Particle Simulator (Mars-AMPS) code. The framework of the coupled Mars-AMPS and MTGCM codes is addressed in detail in Paper I and *Valeille et al*. [2009a, 2009b]. The first application of this coupling of the 3-D AMPS (earlier version of our current model) [*Tenishev et al*., 2008] with the MTGCM has been successfully completed by a series of studies on the hot O corona [*Valeille et al*., 2009a, 2009b, 2010a, 2010b].

In the following section, brief descriptions of the 3-D MTGCM and our 3-D AMPS are provided. Section 3 describes the mechanisms for production of hot C in the Martian upper atmosphere and variations in the background atmosphere. Finally, the detailed investigation of the Martian hot C corona for different solar activities and seasons is presented in section 4, and we discuss conclusions in section 5.

2. Models

2.1. Mars Thermosphere General Circulation Model

As a 3-D finite difference primitive equation model, the MTGCM is a self-consistent atmospheric model for time-dependent neutral temperatures, neutral ion densities, and three component neutral winds over the globe [*Bougher et al*., 1999, 2000, 2002, 2004, 2006, 2009]. The MTGCM is currently an upward coupling model that is driven from the NASA Ames Mars general circulation model (MGCM) code [e.g., *Haberle et al*., 1999] at the 1.32 μbar level (~60–80 km, depending on season). This coupling allows a realistic description of the Martian

lower atmosphere to the MTGCM regime by including continuous effects of the migrating and nonmigrating tides and the seasonal effects of the expansion and contraction of the lower atmosphere [*Bougher et al*., 2006, 2008, 2009]. The major neutral species (CO_2, CO, N_2, and O), selected minor neutral species (Ar, He, and O_2), and photochemically produced ions (e.g., O_2^+, CO_2^+, O^+, CO^+, and NO^+ below 180–200 km) are considered. The MTGCM has its vertical coordinate in log pressure with 0.5 scale height spacing. The prognostic fields for these species are simulated on 33 pressure levels above 1.32 μbar (~70–300 km; for solar maximum conditions) with a 5° × 5° latitude and longitude grid resolution. In the lower thermosphere where CO_2 is the dominant species, the scale heights are about 7 km–10 km. This translates to a vertical spacing of ~ 3.5 km–5 km in the lower thermosphere. In the upper thermosphere, O surpasses CO_2 as the dominant species at ~ 200 km on the dayside. Due to the impacts from the change in season and solar activity, a range of dayside scale heights at ~200 km is 16 km (low solar activity) to 28 km (high solar activity). Thus, the vertical spacing in the upper thermosphere ranges from ~ 8 km to 14 km. The important feedback of the simulated O atoms upon CO_2 cooling rates is captured by implementing a fast non-local thermodynamic equilibrium (non-LTE) 15 μm cooling scheme with corresponding near-IR heating rates [*Bougher et al*., 2006; *López-Valverde et al*., 1998]. The key parameters for the Martian seasons and solar cycle variations can be adjusted to customize the MTGCM cases (e.g., solar high/low, aphelion/equinox/perihelion for this study) for different purposes of the study.

2.2. Mars-Adaptive Mesh Particle Simulator

As described in great detail in Paper I, the Direct Simulation Monte Carlo (DSMC) [*Bird*, 1994] method, a standard numerical method today, stochastically solves both the linear and nonlinear Boltzmann equations. The transition from a local thermodynamic equilibrium (LTE) region to a non-LTE region occurs in the tenuous upper atmospheres of the planets, where it becomes challenging to model the physics of the gas distributions. The DSMC method allows solving the often intractable Boltzmann equation by describing the collisional dynamics of a finite number of model particles in the rarefied gas flow regime. Using the method allows the incorporation of complex physical processes without a significant complication of the numerical procedure.

The DSMC method separates the translational motion of species from the intermolecular and uses a Markov chain scheme to describe the evolution of the velocity distribution function. The total collision frequency is a key quantity in the development of the relaxation scheme of the model. The probabilistic relaxation scheme is based on a representative sampling of actual intermolecular collisions. The postcollision velocities are computed in accordance with the laws of the conservation of mass, momentum, and energy in every interaction. The Monte Carlo simulation then computes an averaged value of macroscopic functions, including density, velocity, and flux, over defined regions of phase space using the usual definitions from standard kinetic theory.

Developed within the frame of the DSMC method, the University of Michigan Adaptive Mesh Particle Simulator (AMPS) code [*Tenishev et al*., 2008, 2013] simulates an ensemble of model particles and captures the complicated physics in the distribution of the gas species. The AMPS code is generic and applicable to a wide range of kinetic problems. For a particular purpose, such as modeling the Martian hot atomic corona for this study, AMPS can be run in a test particle Monte Carlo mode with stationary background atmosphere. The test particle Monte Carlo mode does not take into account the intermolecular collisions and allows reducing computational resources and time. For the full consideration of the intermolecular collisions, the full DSMC mode is required, which has been run for cometary coma simulations [e.g., *Tenishev et al*., 2008].

In the application of the AMPS code for the Martian hot corona (Mars-AMPS), the thermosphere and ionosphere for the cases considered are presimulated by the MTGCM and supplied as input values to our Mars-AMPS. Each hot particle in this coupled framework between Mars-AMPS and the MTGCM travels within the influence of the planet's gravitational field and collides with background species before escaping to space or being thermalized in the thermosphere. The type of possible collisions with a nascent hot particle can be either a collision between a hot particle and background species or a collision between hot particles. In our model simulation, we consider only the former collision case, since the collision frequency of the latter case is negligibly small in the Martian upper atmosphere. All scatterings occurring between a nascent hot C and background species in our simulation are assumed to be elastic hard sphere encounters. The collision cross sections for both C_{hot}–O_{cold} and C_{hot}–$CO_{2,cold}$ are not available at present. Therefore, we treated hot C atoms as hot-O-atom-like atoms with the mass and radius of C. The adopted collision cross section is

3×10^{-15} cm^2, which is used by *Ip* [1988] and *Lammer and Bauer* [1991] for O_{hot}–O_{cold} and O_{hot}–$CO_{2,cold}$. The assumption of the same collision cross section for both background O and CO_2 has been employed by the previous hot O studies [e.g., *Lammer and Bauer*, 1991; *Hodges*, 2000; *Valeille et al*., 2009a, 2009b, 2010a, 2010b]. As a test run, we have tried a different description of collision that treats CO_2 as three O atoms. Since CO_2 is a linear molecule, we have adopted twice the C_{hot}-O_{cold} cross section as a reasonable cross section on the average. The resulting total escape rate is decreased by a factor of ~2.6, implying the importance of the choice of cross sections. Due to the fact that thermalization is a key factor for the loss process of hot population, our model will adopt any new improvement in the collision scheme or cross section if there requires further modification for a more realistic description in the future.

The AMPS code utilizes the technique of adaptive mesh refinement (AMR) [*Berger and Colella*, 1989], which allows efficient computation when the cell size is the smallest only where the important production of hot particles and the interaction between nascent hot particles and background atmosphere takes place. The cell size in our computational domain varies based on the sizes of the lowermost and uppermost cells. Without loss of generality, the size of the domain is predetermined in the initialization process, which is typically set to about 2–3 Mars radii without overestimating the escape or overusing the computational time and resources. The nominal cell size varies from about 80 km at the bottom of the computational domain to about 300 km at the outermost part of the domain for the case of 2 Mars radii as the domain size. If one is not interested in sampling macroscopic values during a simulation, the size of the cell in the mesh does not matter in our model. However, sampling quantities become difficult with the large cell size, since the physical situation of macroscopic values (e.g., the density structure of CO^+ and altitude variation of the collision frequency of a hot particle with the background species) often exhibits sharp gradients in their altitude variation at low altitudes (~80–200 km) (Paper I). Increasing the resolution of the mesh will allow sampling these features, but the computation in 3-D cubic cell mesh will become too expansive. In order to avoid this problem, we overlay an auxiliary mesh, which is in spherical coordinate, on our Cartesian coordinate mesh. As described in detail in Paper I, this mesh is used as a tool for sampling and visualization of particular macroscopic features without increasing the computational time and resources. The CPU times required to run a typical simulation for a particular solar condition and seasonal case with the computational domain size of 2 Mars radii on 48 processors are ~7–8 h for the photodissociation of CO case and ~$<$1 day for the dissociative recombination of CO^+ case. Longer CPU time is needed for the dissociative recombination of CO^+ case due to the extrapolation scheme for the CO^+ density in the upper atmosphere (detailed description in Paper I).

3. Description of Background Atmosphere

We have computed the total global escape rate of hot C resulting from two photochemical mechanisms, photodissociation of CO and dissociative recombination of CO^+, for different solar cycle conditions and Martian seasons. A hot C atom is produced with the excess energies in photodissociation of CO,

$$CO\left(X^1\Sigma^+\right) + h\nu \rightarrow C\left(^3P\right) + O\left(^3P\right),$$

in accordance with the photodissociation frequencies adopted from *Fox and Black* [1989].

Dissociative recombination of CO^+ produces a hot C atom in five possible energetic channels of the form

$$CO^+ + e \rightarrow C + O + \text{excess KE}.$$

See Paper I for the detailed information of the individual channels. The consideration of different cases allows characterization of the important thermospheric and exospheric asymmetries and the circulation in the Martian upper atmosphere under the influences of the solar flux variations.

In this study, the solar cycle and seasonal variability of the hot C corona are presimulated in the MTGCM (yielding thermosphere and ionosphere fields), utilizing parameters specifically chosen for the Martian seasonal and solar cycle conditions. The two solar cycle cases considered are for low ($F_{10.7} = 70$) and high ($F_{10.7} = 200$) solar activity conditions. The seasons are represented by three different orbital positions of Mars, which are aphelion ($L_s = 70°$), equinox ($L_s = 180$), and perihelion ($L_s = 250°$) corresponding to summer, autumn, and winter in the northern hemisphere, respectively. These conditions are categorized into five cases: perihelion solar low and high (PL and PH), equinox solar low and high (EL and EH), and aphelion solar low (AL). The solar cycle variability is effectively evaluated by a comparison between the solar low and high cases

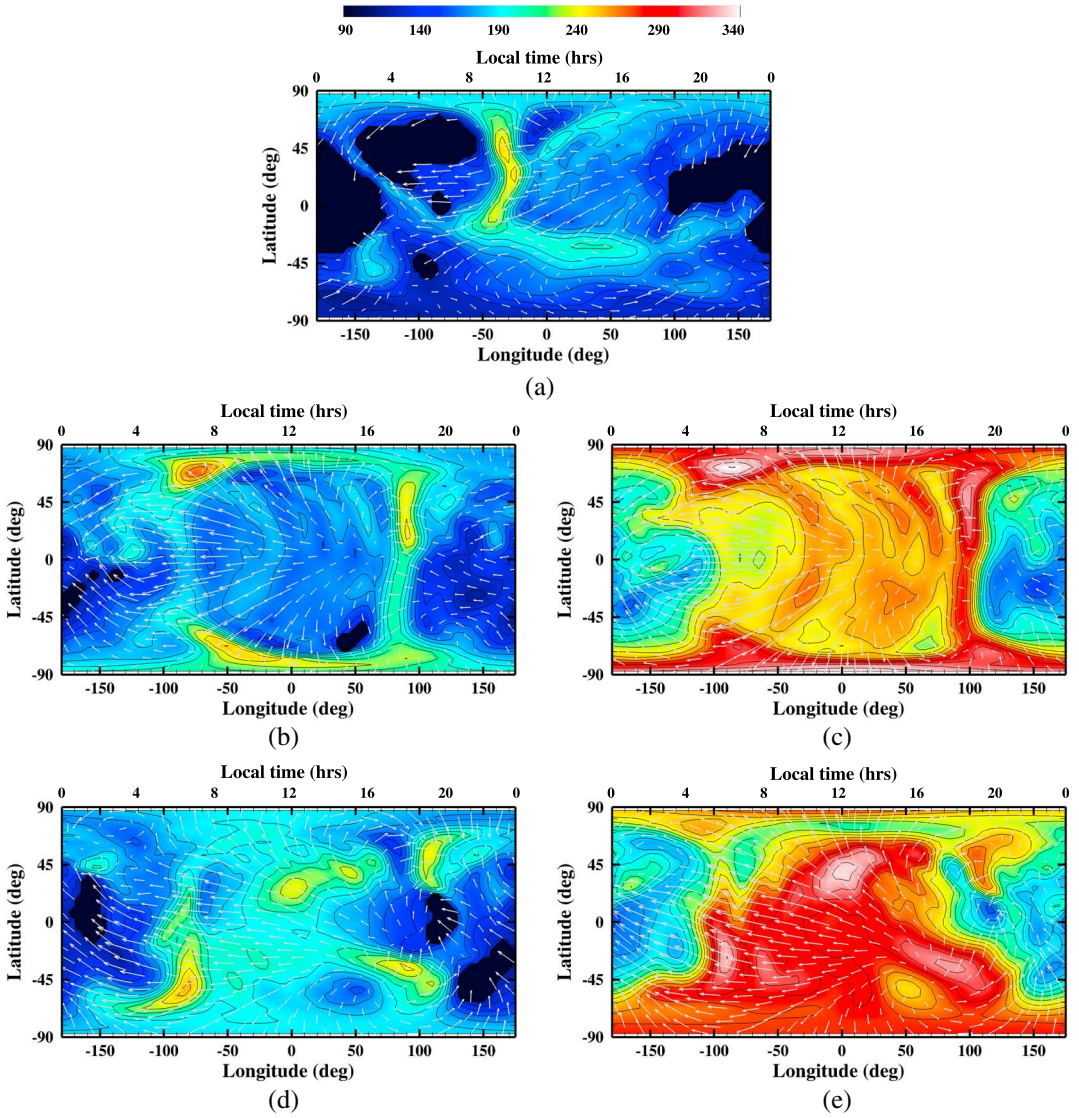

Figure 1. Neutral temperature (T_n) distributions near 200 km (the lower exosphere) for the (a) AL, (b) EL, (c) EH, (d) PL, and (e) PH cases. The global winds are indicated by white arrows. The contours show the temperatures in units of K.

(EL and EH or PL and PH). Since our aphelion case does not have a solar high condition, the seasonal variability is evaluated by a comparison of solar low cases, AL, EL, and PL only. This suite of cases is the same as those investigated by *Valeille et al*. [2009b] for the variation of the hot O exosphere at the current epoch.

3.1. Temperature and Wind Variation

As a response to the increase in the $F_{10.7}$ index, the magnitude of the neutral temperature increases. However, the horizontal variations of temperature retain the same spatial structures from low to high solar activity conditions as shown in the EL (Figure 1b) and EH (Figure 1c) cases or the PL (Figure 1d) and PH (Figure 1e) cases. According to *Bougher et al*. [1990, 1999, 2009], the Mars thermospheric circulation serves as an efficient thermostat that regulates the dayside temperature driven by solar EUV heating. The global winds play a vital role in modifying thermospheric temperature [*Bougher et al*., 2000]. Upwelling diverging winds adiabatically cool the dayside and subsiding converging winds heat the nightside. This dynamics effectively redistributes the heat in the day-night flow reducing the enhancement of the diurnal contrast. The larger contrast seen in the contour plots on the dayside implies the faster response of the dayside temperature to the advance of the solar cycle, which increases the temperature by about 80–100 K, while the nightside temperature increases by about 40–60 K.

Much more than on Earth, the Martian seasons are defined also by the change in heliocentric distance due to its highly elliptical orbit as well as its rotational axial tilt of about 25°. Over the course of the Martian year, the solar EUV flux reaching the top of the thermosphere varies by about ±22% due to the elliptical orbit of Mars [*Bougher et al*., 1990]. As a result, the temperature and global circulation structures change significantly. The peak dayside temperatures vary from about 240 K for the AL case (Figure 1a) to about 260 K for the PL case (Figure 1d). The high-temperature regions are situated in the middle latitudes LT = 10:00 for the AL case. For the EL case (Figure 1b), the high-temperature region expands to the morning and evening terminators and the high latitudes near the polar regions and emerges toward the southern hemisphere for the PL case with the highest temperatures located in the middle latitudes on both hemispheres. Due to the less pronounced day-night pressure gradient, diurnal temperature variation is about 80 K for the AL case while this variation is larger in the PL case, which it is about 120 K. In general, MTGCM horizontal winds diverge from midafternoon at the subsolar latitude, flow strongly across the terminators, and converge on the nightside. During equinox, dayside meridional winds diverge from low latitudes, flow strongly across both poles, and converge on the nightside at low to middle latitudes. During solstices, the dayside meridional flow is generally from the summer toward the winter pole, with nightside convergence at winter hemisphere middle to high latitudes. As a consequence, this yields the existence of thermal O peak densities in winter poles, implying the winter polar warming effects at Mars. Detailed description of this implication is presented in the next section by O/CO_2 ratio at two extreme conditions: aphelion/solar low activity and perihelion/solar high activity.

3.2. Neutral Atmosphere Variation/CO Density Distribution

CO_2 is the major neutral species in the Martian thermosphere up to an altitude of between ~180–220 km, depending on solar activity and season. As discussed in detail in Paper I, O becomes more responsive to the global atmospheric circulation than CO_2 does, resulting in an enhanced O population on the nightside where the convergence and downwelling of the circulation occur. CO is an important neutral species that also exhibits some density enhancement on the nightside like the O density. However, in general, CO responds more closely to the local background temperature distribution like the CO_2 density. These different global responses from different neutral species uniquely define their own horizontal distributions, which are important for the overall structure and shape of the thermosphere, ionosphere, and hot corona.

The left columns in Figures 2a, 2b, and 2c show the horizontal distributions of O, CO_2, and CO, respectively, for low and high solar activity conditions at equinox at an altitude near 200 km. The CO density is spatially distributed in a pattern that combines features of both the O and CO_2 density distributions. For the low solar activity case, the maxima of the CO density are located near the polar regions on the morning terminator, and the minima are situated mostly on the nightside at low-latitude region. When solar activity increases, the spatial distribution retains much the same pattern, but the whole thermosphere is enhanced by the increase in the solar EUV flux, resulting in an increase in the CO density by a factor of ~7.5 at the subsolar point.

The seasonal influence is quite strong on the spatial distributions of the neutrals. Two extreme cases, the AL and PL cases, for O, CO_2, and CO are shown in the right columns in Figures 2a, 2b, and 2c, respectively. For the AL case, the O concentration reaches a maximum at the south pole, which is the winter pole during aphelion, while the CO_2 concentration has its maximum near the north pole. For the PL case, the O maximum is located near the north pole, the winter pole during perihelion, on the nightside, and the CO_2 maximum is on the dayside near the south pole. These characteristic special distributions of O and CO_2 also appear in the CO distribution pattern. The maxima and minima of CO_2 and CO are correlated in most of the places over different seasons.

Figure 3 shows the seasonal variation of the O/CO_2 ratio. The overall bulk flow of the atmosphere is the summer-to-winter interhemispheric flow during both perihelion and aphelion, with an upwelling vortex circulation toward the summer pole. This flow converges in the winter polar region on the nightside. The adiabatic heating from this subsiding flow is dominant during perihelion, due to the stronger meridional winds, showing another implication of the winter polar warming at Mars [*Bougher et al*., 2006].

3.3. CO^+ Ionospheric Peak and Its Distribution Compared With O_2^+

CO^+ is one of the major ionospheric species that is mainly produced by photochemical processes. CO^+ is predominantly produced through photoionization of CO and photodissociative ionization of CO_2, which are

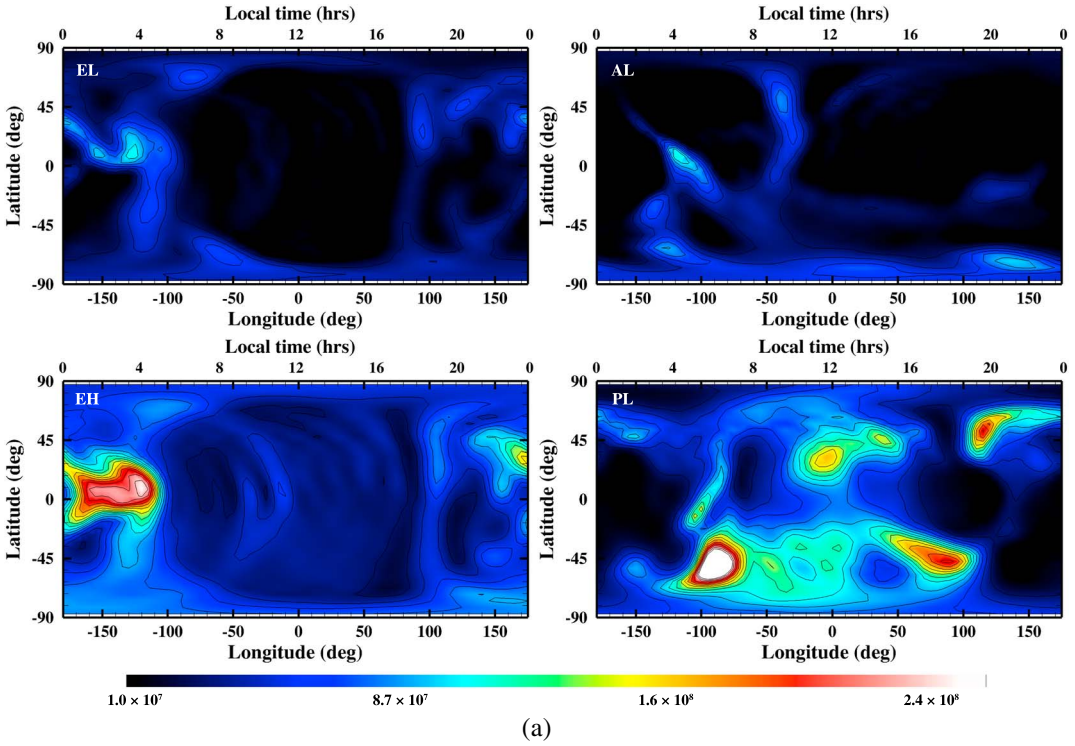

(a)

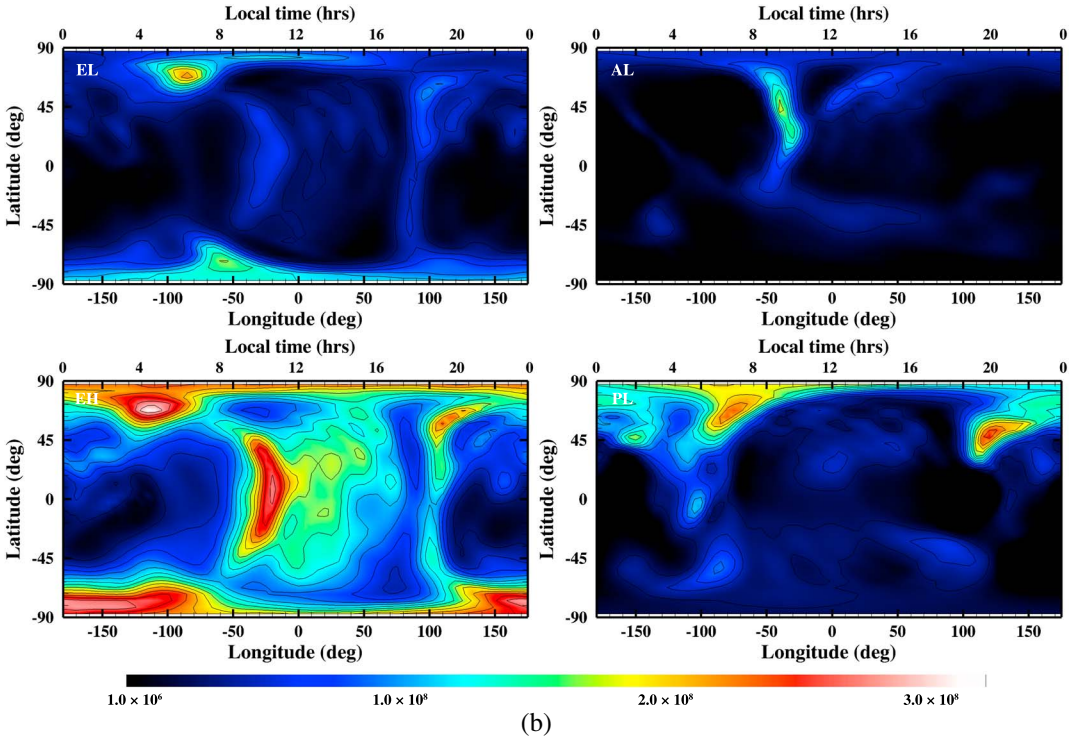

(b)

Figure 2. Thermal (a) O, (b) CO_2, and (c) CO density distributions near 200 km (the lower exosphere) for the (top left) EL, (top right) EH, (bottom left) AL, and (bottom right) PL cases.

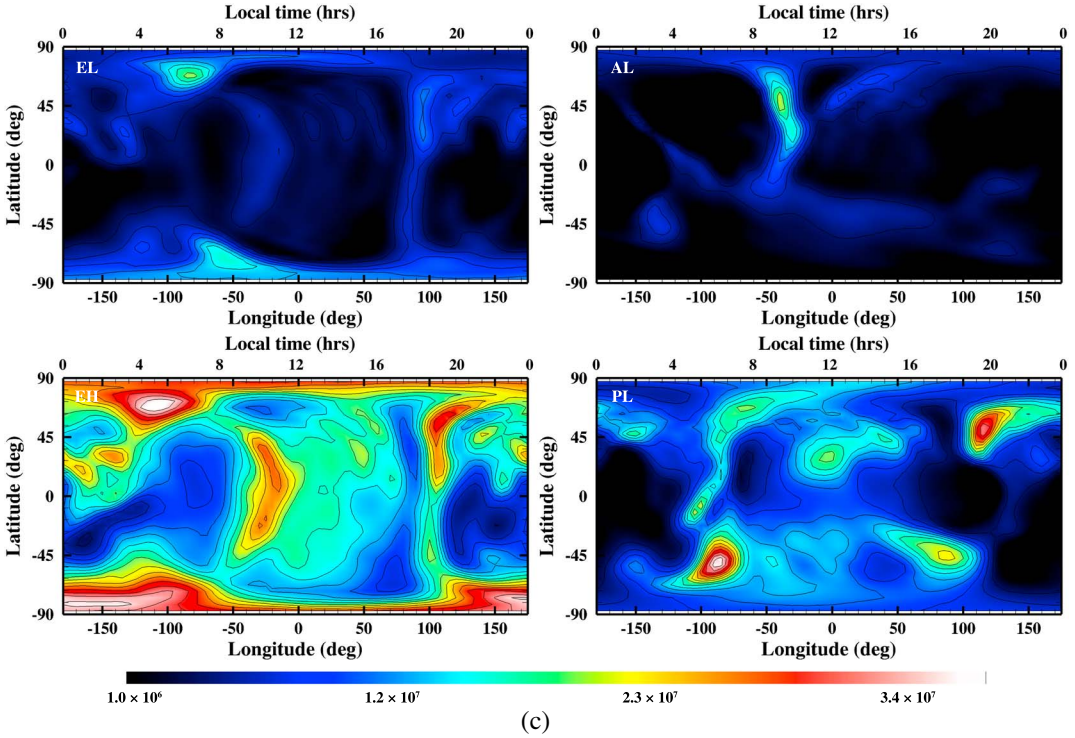

Figure 2. (continued)

highly sensitive to the solar EUV flux in the upper atmosphere. The newly produced CO^+ ions quickly charge exchange with CO_2 deep in the thermosphere, forming a horizontal distribution pattern that is anticorrelated to that of O_2^+ (detailed descriptions in Paper I).

The CO^+ ion distribution differs from that of the major ion, O_2^+, in several ways. O_2^+ is generated through charge exchange between CO_2^+ and O, where their source reactions are directly related to the densities of the local background O and CO_2. The main removal process for O_2^+ is dissociative recombination of O_2^+, which allows O_2^+ to have similar solar cycle and seasonal variability as that of neutral background species. However, CO^+ displays inverse behavior because its loss process is tightly related to the local CO_2 density. Consequently, the resulting hot C density distribution exhibits different horizontal distribution than that of hot O. The peak altitude of the CO^+ density occurs at high altitudes because the major loss processes in the ionosphere are reactions with neutral species [*Fox and Sung*, 2001]. The ionospheric peak of CO^+ is located at an altitude of approximately 210 km and 240 km for low and high solar activity at equinox, respectively (Figure 4a). Compared to the O_2^+ peak height (~135 km) (Figure 4b), the CO^+ density near its peak height is more sensitive to solar activity variation since the density peak is situated where the solar EUV radiation is more effectively absorbed by the background atmosphere.

The altitude range of the CO^+ density from the MTGCM does not include the density peak of CO^+. All the densities of the thermospheric and ionospheric species from the MTGCM except for CO^+ exhibit peak altitudes below 200 km, which allows extrapolation of the densities above 200 km with respect to the local scale height. However, to capture the relatively high peak altitude of the CO^+ density, the modification of our extrapolation scheme is required. We adapted the features of the CO^+ density profiles from the previously published studies [*Fox*, 2004; *Fox and Bakalian*, 2001; *Fox and Haćić*, 1999, 2009] (i.e., peak altitudes and scale heights for low and high solar activity). We assumed that the CO^+ density increases exponentially above the upper boundary of our input ionosphere up to the adapted peak altitude and decreases with the adapted scale height. In order to describe the seasonal variation of the CO^+ density above 200 km, we parameterized the density as a function of the atmospheric pressure. As shown in Figure 4a, this description of seasonal variation results in a relatively higher and lower peak altitude for the CO^+ density at perihelion and aphelion, respectively, than that at equinox.

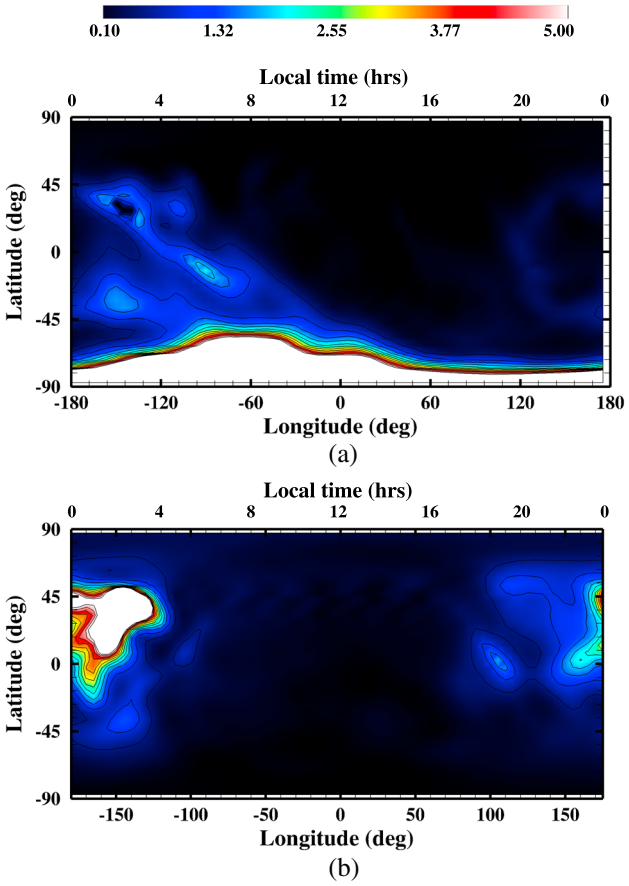

Figure 3. The horizontal variation of the O/CO_2 ratio for the (a) AL case and the (b) PH case. The O/CO_2 ratio is obtained at an altitude of 160 km and 200 km (nominal altitude for the base of the exosphere) for the AL and PH cases, respectively. For the AL case 160 km is chosen to show any range of values.

A change in solar activity, which can be characterized as a variation of the solar EUV flux, expands the thermosphere and ionosphere and enhances the local background densities. The overall magnitude of the ionospheric density increases by about an order of magnitude over the dayside as solar activity increases. The magnitude of the O_2^+ peak density is enhanced from low to high solar activity conditions, while the peak height of O_2^+ in the lower thermosphere does not appreciably change; i.e., altitudes near/below ~120 km are subject to the solar IR flux, which do not vary over the solar cycle [*Valeille et al.*, 2009b]. On the other hand, CO^+ displays different responses to the solar EUV flux variation due to its different characteristic altitude profile in the upper atmosphere. As explained in Paper I, the nominal density peak of CO^+ is located above 200 km for both the low and high solar activity cases because of its parent sources and production and loss reactions. The upper atmosphere will be more affected by the solar EUV flux than the lower atmosphere, and the CO^+ density near its peak changes according to the mixing ratio of the parent sources. As a result, both the peak height and the magnitude of the peak of CO^+ are highly variable with the change in the solar EUV flux. Figure 5a shows the horizontal variation of the CO^+ density near 200 km altitude for low and high solar activity at equinox. The maximum density is situated at the equator near on the morning terminator, showing the anticorrelation with the O_2^+ density distribution.

The seasonal responses in the thermosphere and ionosphere are characterized as the expansion of the lower atmosphere mostly by the IR flux. The solar IR flux on Mars varies as heliocentric distance changes. Because the O_2^+ density peak is located where the ionosphere is influenced more by the IR flux, seasonal variability is apparent in O_2^+ by its peak height varying by 12–15 km from the AL case to the PL case [*Valeille et al.*, 2009b]. In contrast, the effect of the seasonal change on the CO^+ density is prominent at high altitudes due to the different source dependency in the thermosphere. As shown in Figure 4a, the production of CO^+ is maximized in the upper atmosphere where IR radiation is not effectively absorbed. As a consequence, the CO^+ density is affected more by the variation in the EUV flux than the IR flux through the seasons. The magnitude of the CO^+ density increases in response to the seasonal change from the aphelion to perihelion cases as well as the change in the peak altitude by about 20–25 km at low solar activity (Figure 4a). Figure 5b shows the seasonal variations in the horizontal distribution of the CO^+ density at low solar activity. The variation in the magnitude of the density is a factor of about 1.7, when the densities at aphelion and perihelion are compared to that at equinox. Unlike in the case of hot O produced from dissociative recombination of O_2^+, these seasonal variations in the CO^+ density has direct effects on the resulting escape rate of hot C.

The peak altitude of the dissociative recombination of CO^+ varies over different regions due to a couple of factors: the peak altitude variations of the CO^+ and electron densities for solar and seasonal conditions

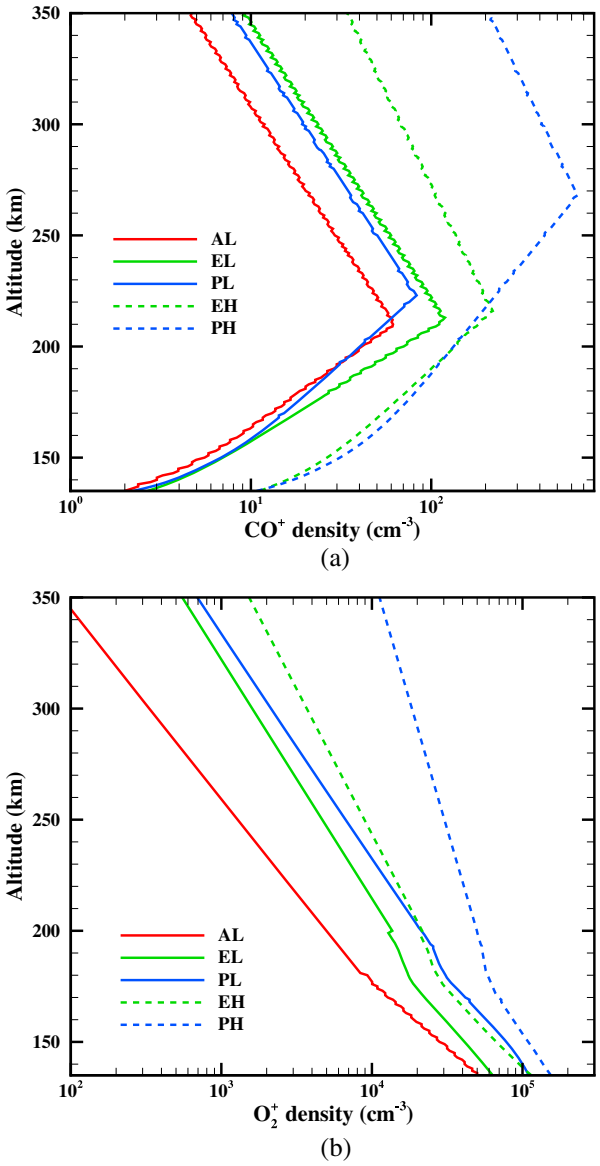

Figure 4. The density profiles of the (a) CO^+ and (b) O_2^+ densities in the background atmosphere for the AL, EL, PL, EH, and PH cases. The densities are extracted at solar zenith angle (SZA) 60° northward along the meridian.

and the choice of rate coefficient. Since we made the exact choice of a rate coefficient, the peak altitude variations of the CO^+ and electron densities are important for determining the peak altitude of the production rate. The scale height of the CO^+ density increases as solar activity increases, while the electron density shows rather small changes in the peak altitude as well as the enhancement in the density. The electron density peaks at an altitude near where the O_2^+ density peaks. The resulting dissociative recombination rate, $\alpha(T_e)n_{CO}+n_e$, is maximized at an altitude where the multiplication of the CO^+ and electron densities is maximized. Therefore, although the peak altitude of the CO^+ density is situated above ~200 km altitude, the production rate of hot C from dissociative recombination of CO^+ peaks nominally at an altitude slightly lower than 200 km.

4. Results and Discussion: Solar Cycle and Seasonal Variability of the Hot Carbon Corona

4.1. Local Features and Structure of the Hot Carbon Corona

We have simulated the global dynamics of hot C and its variations with the solar cycle and seasons. The hot particle criterion in our model is set by the value of $V_{threshold}$. The model particle in the computational domain is determined as a hot species when its speed exceeds the local $V_{threshold}$. The definition of $V_{threshold}$ is not crucial if the model computes the total loss rate of hot species only. However, in the case of estimating the density profile or horizontal distribution of the resulting hot corona, one needs to carefully choose $V_{threshold}$. In our current model, for counting all hot C (i.e., including ones that can be thermalized before they escape), the $V_{threshold}$ is defined as twice the local thermal speed, which is related to the local background neutral temperature [*Valeille et al.*, 2010a; Paper I]. Consideration of slightly larger $V_{threshold}$, such as 1/15 of the escape energy [*Yagi et al.*, 2012], results in the inclusion of about 2% of the hottest end of the Maxwellian distribution of thermal population to hot population, where $V_{threshold} = 2\times$ thermal speed allows $<1\%$. This difference is not critical, but the $V_{threshold}$ that is larger than these values would overestimate the density of hot species and increase the computational resources and time. If one is interested in only the total integrated values, such as the loss rate and escape flux, setting $V_{threshold}$ to even larger value (i.e., escape speed) than our nominal setting will achieve much faster computation without losing accuracy. The effect of the local $V_{threshold}$ variation on the resulting hot C corona as well as the variation in the hot C corona will be described in detail in the following sections. Two dominant source reactions, photodissociation of CO and dissociative recombination of CO^+, display

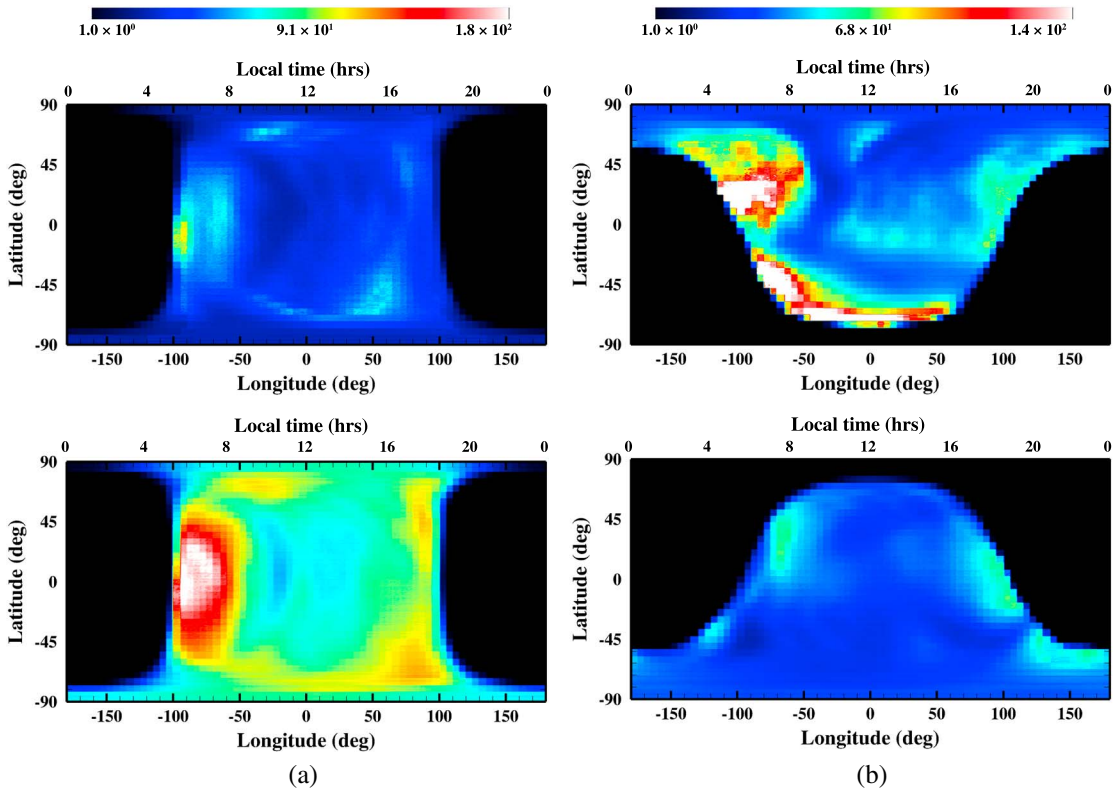

Figure 5. CO^+ density distribution near 200 km (the lower exosphere) for the (a) EL (top) and EH (bottom) cases and for the (b) AL (top) and PL (bottom) cases.

different features in the simulated hot C distributions. Therefore, these two mechanisms are discussed individually in the following sections.

4.1.1. Photodissociation of CO

As discussed in the previous section, CO is spatially distributed in the pattern that resembles elements from that of thermal CO_2 and of thermal O features. Figure 6 shows the variation of hot C density produced by photodissociation of CO for different solar activities at equinox in the noon-midnight meridian plane. While the spatial distribution over the planet does not change significantly as the solar activity advances, the hot C density is enhanced by about a factor of 5–6. As the color contours show in Figure 6, the density distribution peaks

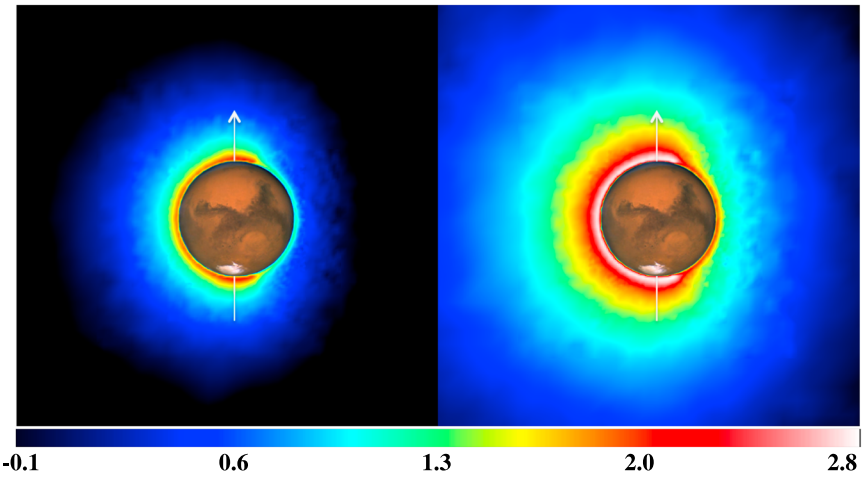

Figure 6. From left to right, hot C produced from photodissociation of CO for the EL and EH cases. Sun-Mars meridian plane with the Sun toward the left. The color scale indicates the log of the hot C density (cm^{-3}).

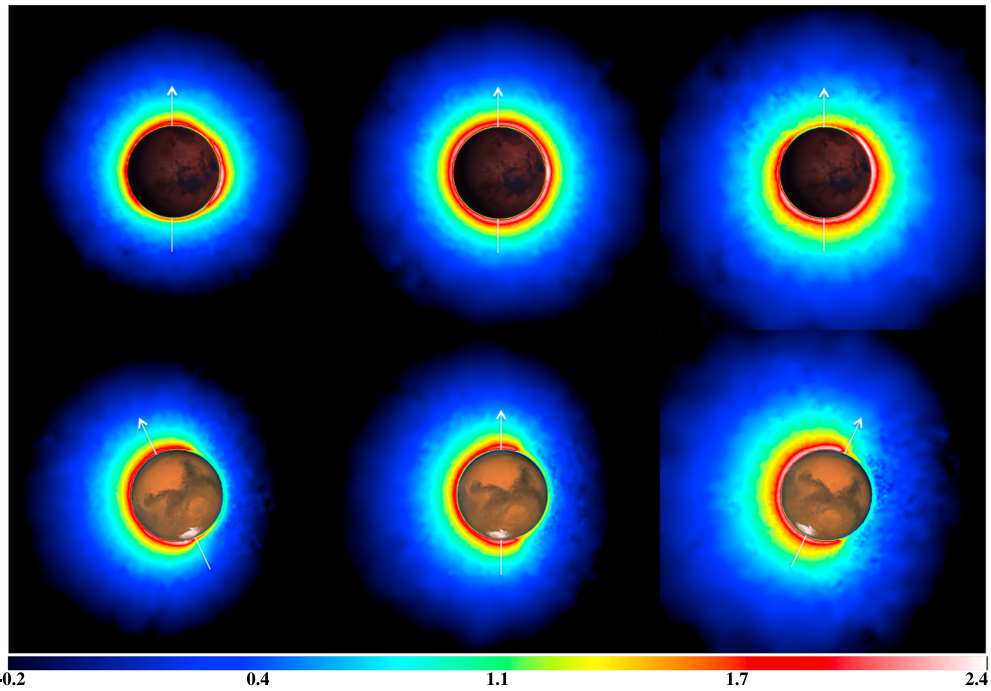

Figure 7. From left to right, hot C density produced from photodissociation of CO for the AL, EL, and PL cases. (top row) Tail-to-Sun view and (bottom row) Sun-Mars meridian plane with the Sun on the left. The color scale indicates the log of the hot C density (cm^{-3}). For the AL and PL cases, this view shows the regions at longitudes of 90° and −90° rather than the morning and evening terminators due to the axial tilt of the planet.

globally on the dayside only and extends over the poles as it decreases by about an order of magnitude on the nightside. The hot density distribution shows an abrupt decrease on the nightside and a tenuous coverage. This existence of low hot C density on the nightside is an important feature due to the effect of gravity on hot C atoms from the dayside, impacting the nightside and scattering back upward [*Valeille et al*., 2009a].

Seasonal variation on Mars is driven by several factors. The variable solar EUV flux due to the large orbital eccentricity of Mars controls the thermospheric circulation. This thermospheric circulation is further modified by upward propagating tidal and/or wave momentum forcing from the lower atmosphere [*Bell et al*., 2007; *Bougher et al*., 2006, 2014]. Seasonal variation is also characterized by the solar IR flux that influences mostly the lower atmosphere, resulting in the expansion/contraction of the lower atmosphere. Variable dust loading (episodic dust storm evolution) also contributes to this seasonal expansion/contraction [*Bougher et al*., 2014; *Forget et al*., 2009]. The coupled framework between the MTGCM and the NASA Ames MGCM allows the seasonally specified dust opacities in the MGCM lower atmosphere to impact the thermospheric structure in the MTGCM code. Therefore, constant pressure levels in the MTGCM change in altitude as seasons advance, in accordance with the dust loading prescribed within the MGCM.

CO becomes an important neutral background species above an altitude where O is a dominant neutral species; this altitude ranges from ~190 km to 240 km, varying with solar activity and seasons. In this altitude range, the thermalization of nascent hot C atoms becomes locally minimized due to the decrease in the densities of the collision partners, O and CO_2, in the background atmosphere. The seasonal variability of the resulting hot C density (Figure 7) is a factor of about 1.2–2.1 at the subsolar point in the AL and PL cases compared to that in the EL case, respectively. This variation implies that the seasonal variation in the hot C corona is characterized as changes in the spatial distribution and structure of the density profiles of hot C but significantly milder enhancement in density than the solar cycle variation.

Among the several factors that affect the hot C density enhancement near the winter poles, neutral temperature and background thermospheric CO and O play the major role, with atmospheric circulation serving as a minor role. As illustrated in Figure 7, the meridian plane view of the density distribution does not display distinctive differences over the seasons, except for the enhancements near the south and north poles

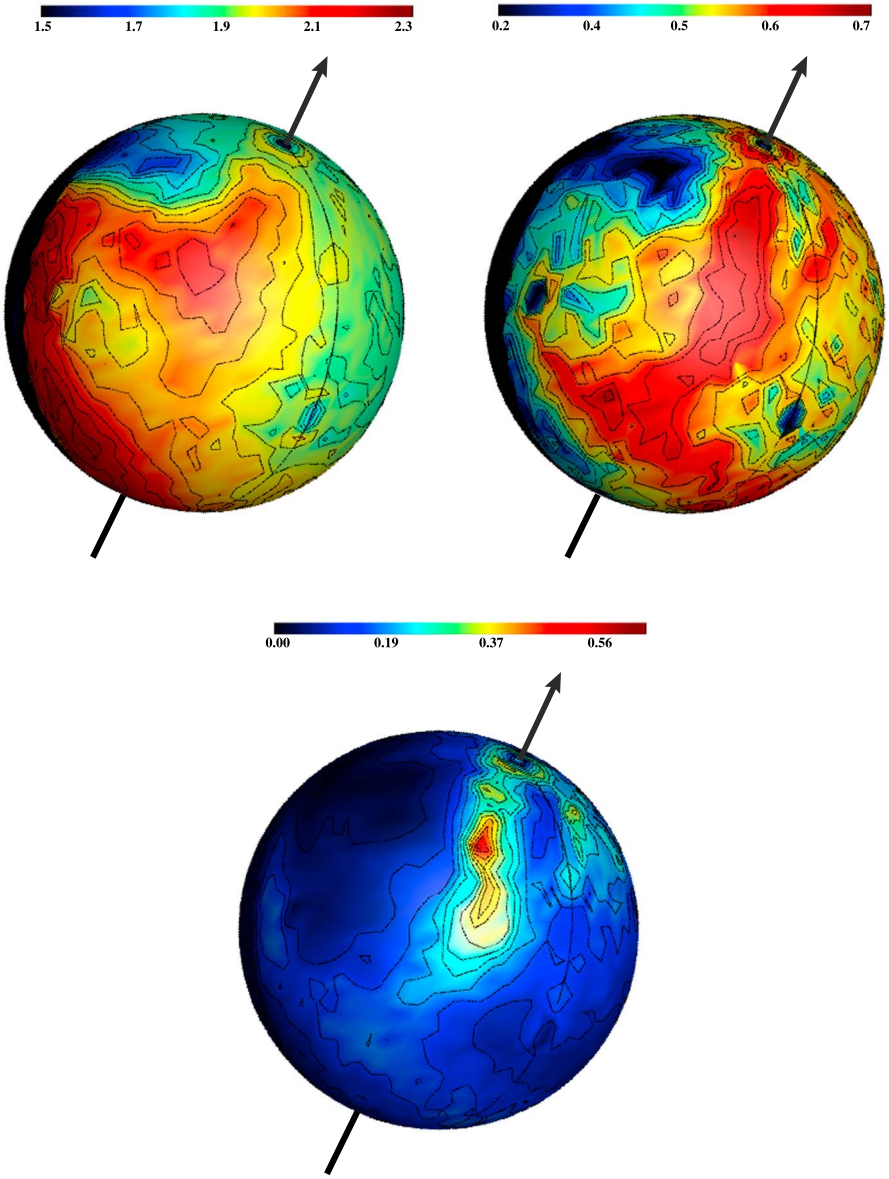

Figure 8. Longitude-latitude variation of (a) hot C density (in unit of log (cm^{-3})) with $V_{threshold}$ = local thermal speed, (b) hot C density with $V_{threshold}$ = escape speed, and (c) collisional frequency (in unit of s^{-1}) between background species and hot C from photodissociation of CO for the AL case at an altitude of 200 km. The planet is rotated to show the region around LT = 09:00. The Sun is located on the right.

for the AL and PL cases, respectively. The seasonal variability is more distinguishable in the tail-to-Sun view as shown in Figure 7. The locations of the highly populated regions change over the seasons, in addition to the global enhancement of hot density as the heliocentric distance changes. According to the map of the neutral temperature at the altitude of the lower exosphere level (Figure 1), some of these highly populated regions correspond to the local minima of the neutral temperature. This feature is a logical result to expect, since the local $V_{threshold}$ is relatively low in the regions of the low neutral temperature (e.g., morning terminator region in the AL and EL cases). The low local velocity criterion allows the addition of the relatively lower velocity population of hot C. This slow hot C does not have enough energy to escape to space and is easily thermalized.

This situation is shown in Figure 8, as an example of the effects of the three-dimensional background atmosphere on the hot corona. The local maxima for hot C with its velocity exceeding twice the local thermal speed are located in different regions from those for the hot C with its velocity exceeding the local escape speed. The local hot C density is maximized along the morning terminator (Figure 8a), where hot C is most

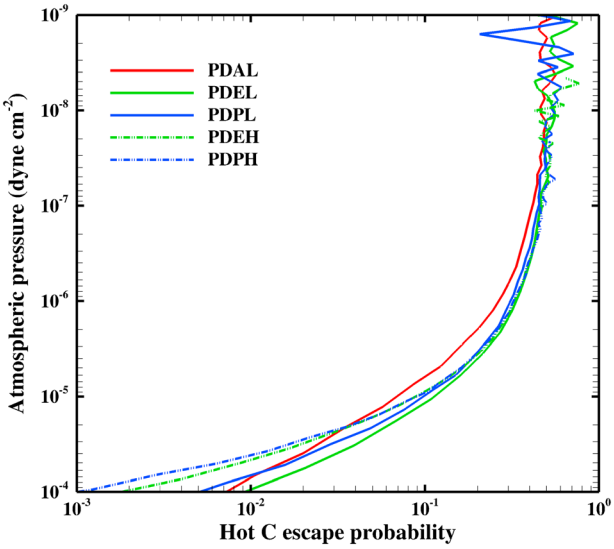

Figure 9. Hot C escape probability for photodissociation of CO case calculated at SZA 60°; 1 dyn cm^2 is equivalent to 1 μbar.

likely to attain relatively lower velocity. This low-velocity hot C does not have enough energy to escape to space and is easily thermalized via collisions with the ambient constituents. Elimination of the low-velocity hot C can be achieved by increasing the $V_{threshold}$ up to escape speed without affecting the calculation of the global escape rate of hot C. The regions where modeled hot C atoms exhibit relatively higher velocity (i.e., exceeding the escape speed) coincide with the regions of higher collisional frequency and maximum hot C production (Figures 8a and 8b: hot C density with different $V_{threshold}$; Figure 8c: collisional frequency). Since relatively large amount of the slow hot C are not counted as hot C atoms when the $V_{threshold}$ = escape speed, the regions with fast hot C and high collisional frequency remain as the maximum hot C regions. These spatial variations of the local macroscopic values, such as the density of the resulting hot species and the local criterion for model particles, are inherently absent in one-dimensional descriptions of the thermosphere and ionosphere. Consequently, the previous models with a spherically symmetric background atmosphere over the dayside could have not well described the local variation of the hot species density.

Thermalization of hot C is determined by the local macroscopic parameters such as the density of collision partners, the speed of a nascent hot C, and background atmospheric temperatures. Hot C that sustains enough energy to escape is produced more in the summer hemisphere, while a relatively large fraction of the nascent hot C is thermalized in the winter hemisphere. In our computational domain, the hot C that attains its velocity below the escape speed, but above the local $V_{threshold}$, travels along ballistic trajectories and falls back to the thermosphere because of the gravity attraction of the planet. These hot C atoms with relatively low velocities populate mostly the altitudes below 190–240 km, beyond which the effects of collision with background atmosphere becomes negligible.

Figure 9 shows the escape probability of hot C resulting from photodissociation of CO for different levels of solar activity and seasonal effects (i.e., AL/EL/PL for seasonal variability and EL/EH and PL/PH for solar cycle variability). The escape probability is plotted as a function of atmospheric pressure to eliminate the effect of atmospheric expansion and to show only the effects of the solar cycle and seasons on the escape of hot C. The level where the slopes of the probability curves change and begin to converge is at a pressure level of ~10^{-5} dyn cm^{-2} (1 dyn cm^{-2} = 1 μbar), which corresponds to 180 km–240 km of altitude ranges for the cases considered in this study. The escape probabilities from all cases converge to 0.5 in the upper atmosphere. In 3-D, 0.5 is the highest escape probability once hot particles reach the collisionless regime in the exosphere, because the radial velocity component of half of the hot population points toward the planet.

Solar cycle as well as seasonal variation is more noticeable in the lower atmosphere than in the upper atmosphere. This indicates that solar cycle and seasonal variations play effective roles in the collision-dominated regime due to the variability of the background properties and hot C source mechanisms. As solar activity increases, the atmospheric pressure at the lower atmosphere also increases. Consequently, at high solar activity, there is more production of hot C, but the escape probability is smaller than that at low solar activity. The computed escape probability decreases by a factor of ~2 below an altitude of ~150 km and 165 km for the equinox and perihelion cases, respectively. However, the hot particles from these altitude regions are not likely to escape to space because of the high collision frequency. The variability of the escape probability by seasons is weaker than by solar cycle. Seasonal variation is attributed to the change in heliocentric distance of the planet and to the variations in the lower atmosphere due to the change in the

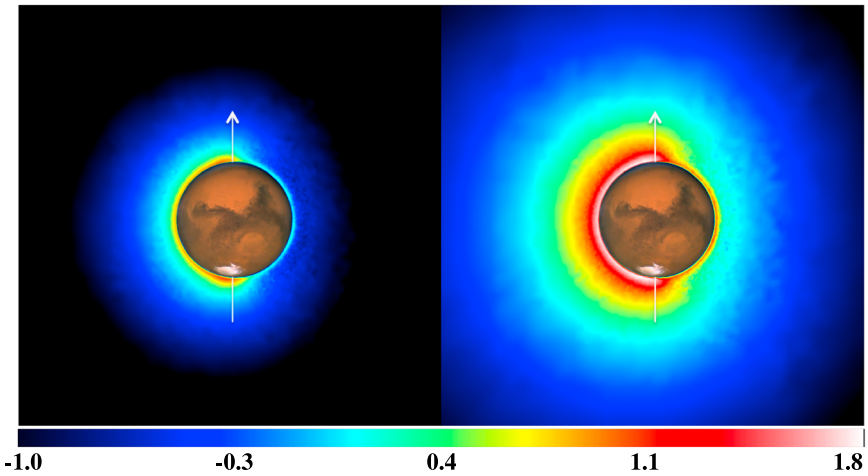

Figure 10. Hot C density from dissociative recombination of CO^+ for the (left) EL and (right) EH cases. Sun-Mars meridian plane is shown with the Sun on the left. Color scale indicates the log of the hot C density (cm^{-3}).

solar IR flux. Like solar cycle variation, the production of hot C at perihelion is higher than other seasonal cases, but the escape probability increases with increasing distance from the Sun.

4.1.2. Dissociative Recombination of CO^+

CO^+ is one of the primary ions in the Martian ionosphere. CO^+ is produced mainly by photoionization of CO and photodissociative ionization of CO_2 and removed predominantly by charge exchange between CO^+ and CO_2. The production rate of CO^+ enhances from the low to high solar activity cases, due to the increase in the CO mixing ratio [*Fox and Sung*, 2001]. As mentioned earlier, the density peak of CO^+ is located at relatively high altitudes, compared to that of the major ionospheric species, O_2^+. This yields direct impacts of the seasonal variation in the CO^+ density to resulting escape rates of hot C, since thermalization is not efficient at such high altitude. On the other hand, the CO^+ density is more variable by solar activity than by seasons, inducing larger solar cycle variability in the production of hot C by dissociative recombination of CO^+.

Figure 10 presents the solar cycle variation of the hot C density resulting from dissociative recombination of CO^+. As in the case of photodissociation of CO, it is logical to expect that the density structure of the resulting hot corona is spatially distributed in a similar manner for the EL and EH cases. The peak densities are located at high latitudes and near the terminator on the dayside, with the minima being on the nightside. The hot C density is maximized near the equator on the morning terminator due to the strong convergence of winds, which is visible in the tail-to-Sun view in Figure 11. The hot C density is enhanced by a factor of about 10–11 as solar activity increases. The nightside density, which is populated due to the return flux of hot C, increases by a factor of 12–13.

The seasonal influence is shown as the shift of the dayside regions toward the summer pole (Figure 11) for the aphelion and perihelion cases. Compared to the equinox case, the hot C density changes by a factor of about 1.3–2 as the heliocentric distance changes, while the density on the nightside varies only slightly. In the tail-to-Sun view, the structural variation of the hot C density profile is more prominent. For the AL case, the production of hot C is high in the high latitudes on the morning terminator, due to the maximum of CO^+ density. The sudden density deficient region corresponds to the region of low electron and CO^+ density. For the PL case, the winter pole and summer pole are clearly distinguishable as in the AL case. The sources for dissociative recombination of CO^+ (i.e., electron and CO^+) are situated mostly on the dayside, which generate this clear distinction between the winter and summer pole.

The escape of hot species is controlled by the two factors: local thermalization and production rate. The enhanced escape is shown in the AL case (Figure 11, in the meridian plane and the tail-to-Sun view) near the southern winter pole, at altitude of about 240 km, and in the high latitudes at the morning terminator. These regions are where the production rate remains substantial, and the collision rate between the nascent hot C and background atmosphere becomes the lowest. Hot C from the "bouncing" effect [*Valeille et al.*, 2010a] has less of a chance to escape to space due to the deceleration and significantly lower collisional frequency.

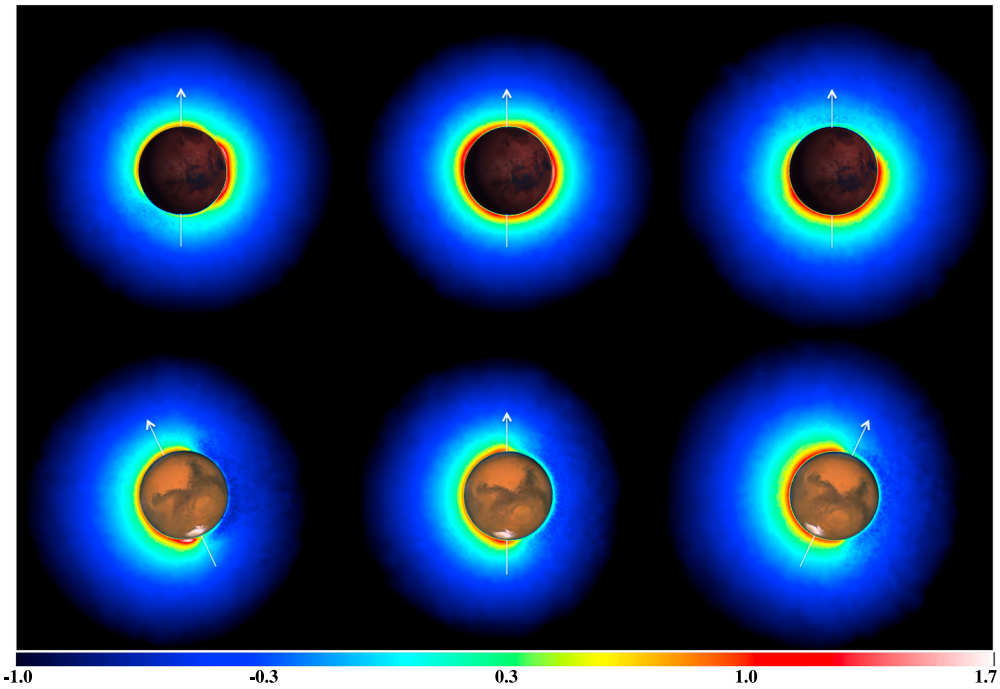

Figure 11. From left to right, hot C density from dissociative recombination of CO^+ for the AL, EL, and PL cases. (top row) Tail-to-Sun view and (bottom row) Sun-Mars meridian plane with the Sun on the left. Color scale indicates the log of the hot C density (cm^{-3}). For the AL and PL cases, this view shows the regions at longitudes of 90° and −90° rather than the morning and evening terminators due to the axial tilt of the planet.

As in the case of photodissociation of CO, the escape probability resulting from dissociative recombination of CO^+ (Figure 12) shows a similar behavior as a function of atmospheric pressure. The seasonal effect on the Martian atmosphere appears as the change in the pressure and density in the lower background atmosphere. The effect of increase in solar activity is characterized not only by the enhancement of the density in the thermosphere and ionosphere but also by the increase in the atmospheric pressure as mentioned earlier. The collisionless regime also shows a shift to slightly higher altitudes in the high solar activity case than in the low solar activity case. The variation of the escape probability for different seasons is not significant in the upper atmosphere. However, the escape probability decreases by a factor of about 1.5–3.5 deep in the thermosphere—below altitudes of ~160 km or 175 km for the aphelion and perihelion cases, respectively.

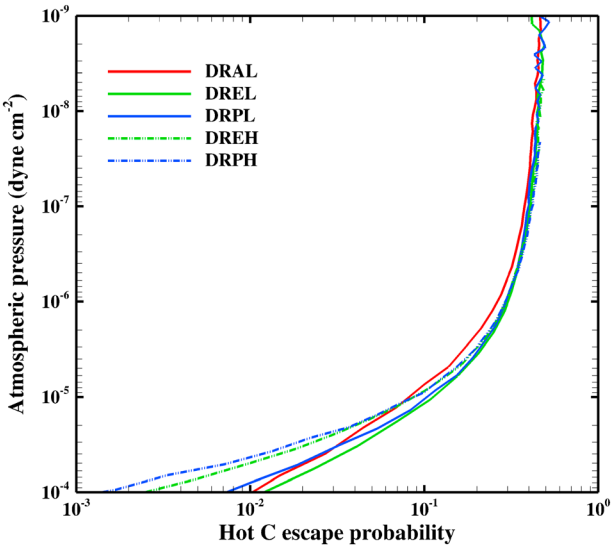

Figure 12. Hot C escape probability from dissociative recombination of CO^+ case calculated at SZA 60°; 1 dyn cm^2 is equivalent to 1 μbar.

4.2. Escape Flux of Hot Carbon

The spatial structure and the magnitude of the escape flux of hot C atoms also exhibit solar cycle and seasonal variations. In the vicinity of the upper boundary of our computational domain, the local macroscopic values, such as the density and velocity of hot population, are averaged over larger volumes than near the base of exosphere, resulting in only small fluctuations in their quantities over the dayside. As a response, the horizontal distribution of the escape flux of hot C also shows the smooth variation.

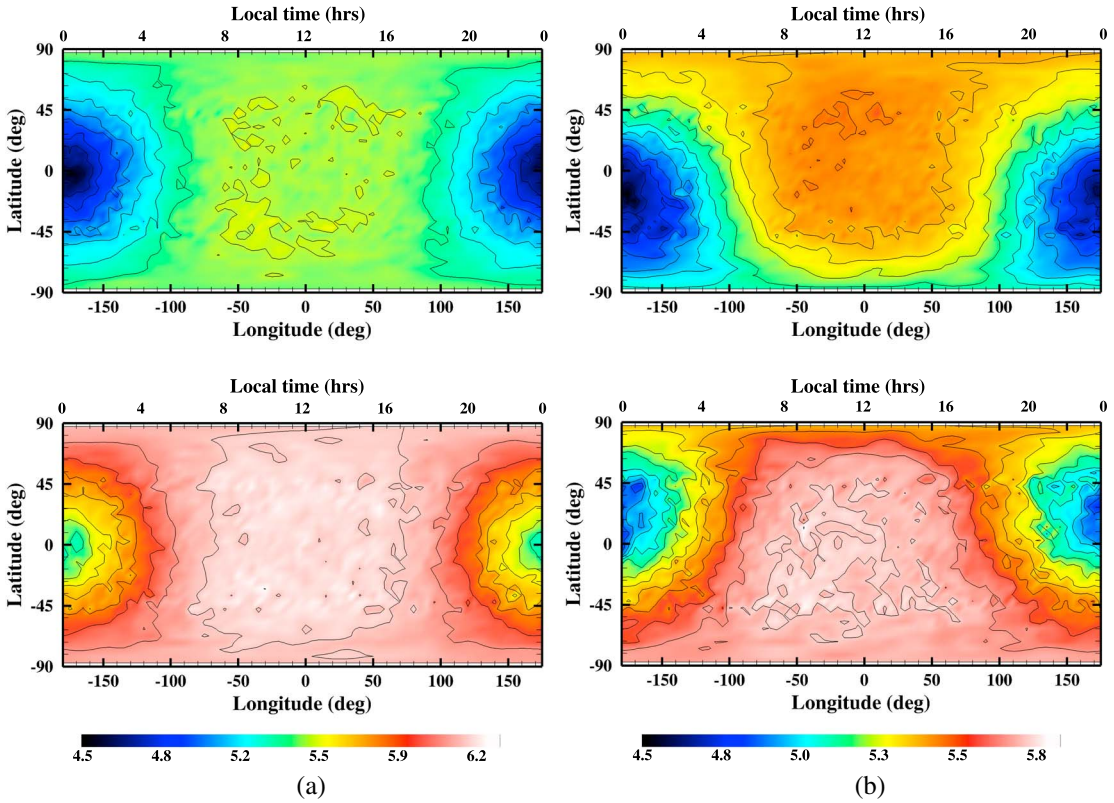

Figure 13. Escape flux of hot C at about 1 Mars radius above the surface (at an altitude of ~3400 km) resulting from photodissociation of CO for the (a) EL (top) and EH (bottom) cases and for the (b) AL (top) and PL (bottom) cases. The contours and color scale show the log of escape flux ($cm^{-2}\,s^{-1}$).

Figure 13a illustrates the effect of the variation in solar activity level on the escape flux resulting from photodissociation of CO at 1 Mars radius above the surface. As for the density distribution, the solar cycle variability does not induce a change in spatial distribution of the low and high escape flux regions but enhances the magnitude of the escape flux as the solar EUV flux increases. The maxima of the escape flux are located at the subsolar point, whereas all the minima are located on the nightside near the anti-subsolar point. The variation in the escape flux over the solar cycle is a factor of about 5–6 on the dayside and about a factor of 6 on the nightside.

The seasonal change in the escape flux is minimal (a factor of ~1.7), but the influence of the planet's axial tilt results in a shift of the subsolar point (coinciding with the location of the maximum flux) toward the summer pole. As shown in Figure 13b (AL and PL), there is a slight regional variation of the magnitude of the escaping atoms over the seasons. The exosphere tends to homogenize the constituents' densities [*Valeille et al.*, 2009b], and hot particles may fall back to the thermosphere before they reach the upper boundary of the computational domain. As a consequence, the spatial gradient of the flux is much milder farther away from the lower exosphere, and the variabilities in the escape flux is smaller than those in the hot C density near the bottom of the exosphere.

Escape fluxes by dissociative recombination of CO^+ for the EL and EH cases are illustrated in Figure 14a. The maximum escape flux regions on the dayside are shown in the regions near the morning terminator at the low to middle latitudes on the southern hemisphere due to the fact that there are more hot C atoms escaping near this region with the relatively low thermalization rate. The escape flux is enhanced by a factor of about 5–6 on the dayside and 4.5 on the nightside. The seasonal variation in the escape fluxes is about a factor of 1.4 moderating the solar cycle influence on the hot C density. The major influence from the seasonal change is on the spatial distribution of the low and high flux regions as shown in Figure 14b.

4.3. Altitude Variations of Hot Carbon, Escape Rates, and Comparisons

We have extracted the profiles of the hot C density produced by photodissociation of CO and dissociative recombination of CO^+ from our 3-D global simulation at a solar zenith angle of 60° in the equatorial east plane,

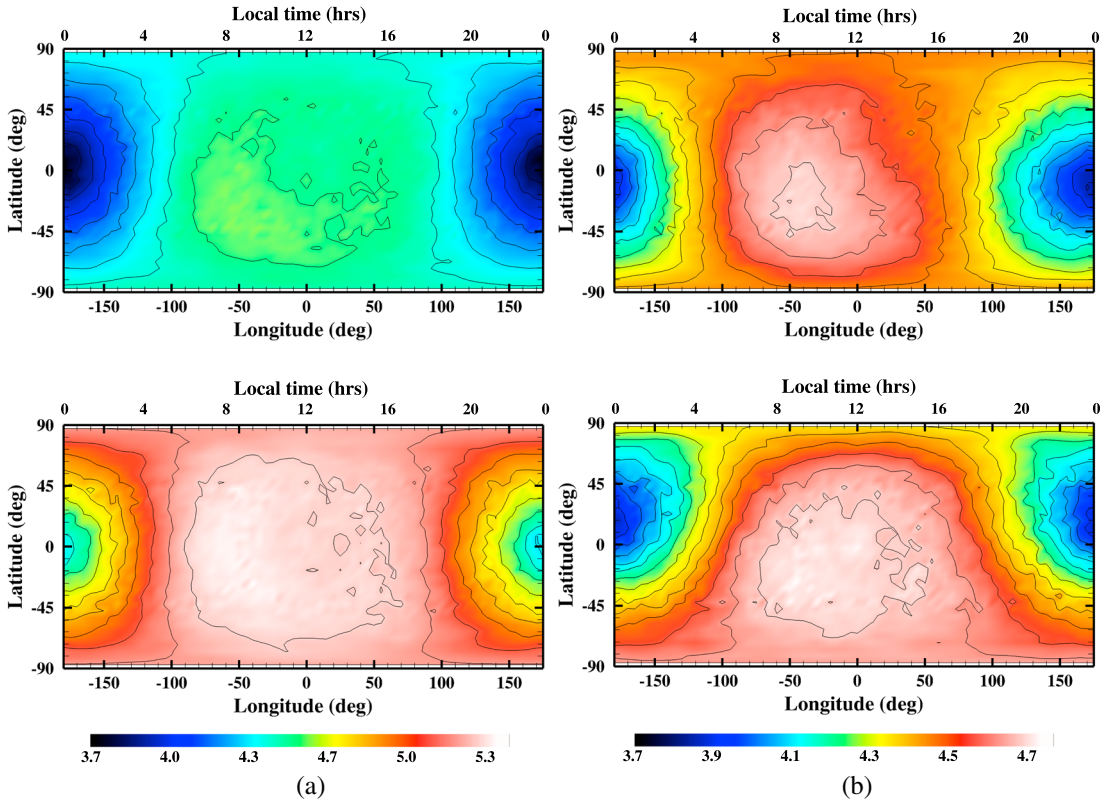

Figure 14. Escape flux of hot C at about 1 Mars radius above the surface (at an altitude of ~3400 km) resulting from dissociative recombination of CO^+ for the (a) EL (top) and EH (bottom) cases and for the (b) AL (top) and PL (bottom) cases. The contours and color scale show the log of escape flux ($cm^{-2}\,s^{-1}$).

which is assumed to be a representation of the dayside average. Several previous models have investigated the hot C component of the Martian corona resulting from various nonthermal source mechanisms [*Cipriani et al.*, 2007; *Fox and Bakalian*, 2001; *Fox*, 2004; *Fox and Hać*, 1999; *Nagy et al.*, 2001]. The direct comparison with our model and the previous models is difficult, since models differ by many aspects such as the description of the thermosphere and ionosphere, numerical scheme, or types of source mechanisms. We here also list the global escape flux from the previous EL model along with the results from the current study and discuss the possible discrepancies to better understand all aspects of the Martian hot C corona.

Figure 15 presents the hot C densities as a function of altitude for the AL, EL, PL, EH, and PH cases from photodissociation of CO and dissociative recombination of CO^+. The relative distances between the density profiles display the seasonal (orbital eccentricity) and solar cycle (solar flux) influences. The simulated hot C is dominantly produced by photodissociation of CO, which is shown as solid curves. The density peaks for both source mechanisms are situated at about 250–300 km, where a large fraction of hot C can escape to space or return to the corona. The ratio of the peak densities of the solar high to low cases for photodissociation of CO is about 4–5.5 and 6.3–7.7 that for dissociative recombination of CO^+. The larger response of dissociative recombination of CO^+ to the solar flux variation is mainly due to the increase of CO^+ production as mentioned previously (i.e., larger CO mixing ratio). Furthermore, the increase in solar flux is resulted in the larger CO^+ scale height and electron density, which increase the dissociative recombination rate.

The seasonal influences are illustrated by the AL, EL, and PL cases (or the EH and PH). The ratios of aphelion and perihelion cases to equinox range from 1.1 to 2 for both source mechanisms. The differences between the three seasons are more apparent at higher altitudes above the lower exosphere (or in the collisionless regime). The density profiles in the lower altitudes between the AL and EL cases are less distinctive and more or less identical. Again, these profiles, however, only represent one particular location on the dayside, and this structure of the lower altitude profiles can be different depending on the local thermospheric and ionospheric conditions. As discussed in the previous section, the study of the seasonal variation needs two- or

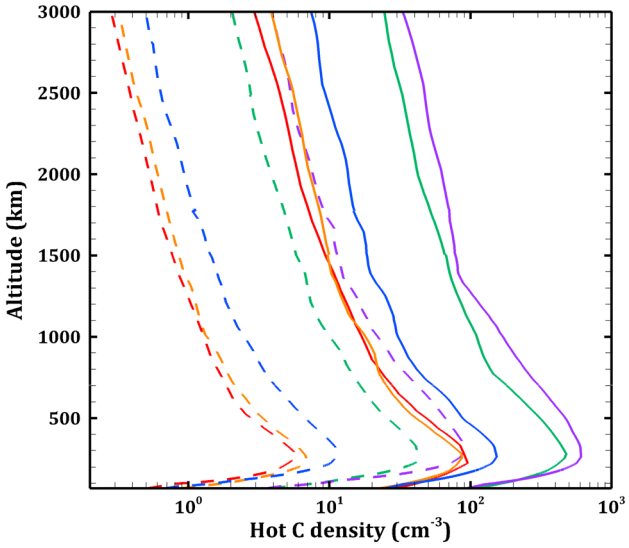

Figure 15. The density profiles of hot C at SZA 60° eastward (along the meridian toward the North Pole) at equator for photodissociation of CO (solid lines) and dissociative recombination of CO^+ (dash lines) for AL (red), EL (orange), PL (blue), EH (green), and PH (purple).

three-dimensional aspects since the seasonal variation impacts the spatial distribution of most of the thermospheric parameters rather than their magnitudes [*Valeille et al.*, 2009a, 2009b]. The seasonal influence is more observable when the dynamics and inherent asymmetries in the atmosphere are incorporated.

We compare our hot C escape fluxes with those calculated by other models. Table 1 lists previous models, their results, and the descriptions of their atmospheric inputs. For comparison purposes, we list our solar low and high cases only (for equinox) and calculate the global escape fluxes at 400 km. *Fox and Hać* [1999] carried out Monte Carlo calculations to compute the velocity distributions of hot C atoms and their global escape fluxes from dissociative recombination of CO^+. Our computed global escape flux for dissociative recombination of CO^+ is about $5.8 \times 10^4\ cm^{-2}\ s^{-1}$ and $2.6 \times 10^5\ cm^{-2}\ s^{-1}$ for solar low and high conditions, respectively. Our escape flux for solar low case is larger by a factor of ~3 than that (eroded case) of *Fox and Hać* [1999], and their solar high case flux is a factor of about 2.2 larger than our value. *Fox and Bakalian* [2001] have estimated the global average escape fluxes of six source mechanisms using the exobase approximation, which are 2.1 and $26 \times 10^5\ cm^{-2}\ s^{-1}$ for low and high solar activity conditions, respectively. In their study, *Fox and Bakalian* [2001] compared their model with the model from *Nagy et al.* [2001]. They also concluded that dissociative recombination of CO^+ has the largest dependency on solar activity. Their separate calculation of the escape flux for photodissociation of CO at low solar activity is about 1.7 lower than our value, $2.8 \times 10^5\ cm^{-2}\ s^{-1}$, but, again, the solar high case value is close to our escape flux (about a factor of 1.1 larger than ours, $1.62 \times 10^6\ cm^{-2}\ s^{-1}$). It is logical to expect the similarity in escape flux at the high solar activity since *Fox and Hać* [1999], *Fox and Bakalian* [2001], and *Fox* [2004] used the MTGCM (one column of the upper atmosphere at a particular location).

Table 1. Comparison of Escape Fluxes Between Current Model for This Study and Previous Models[a]

Models	Low Solar Activity	High Solar Activity	Thermosphere/Ionosphere Model	Numerical Scheme
			Photodissociation of CO	
Nagy et al. [2001][e]	0.27[e]	3.9[e]	1-D	Two-stream method
Fox and Bakalian [2001]	0.165	1.8	1-D	Exobase approximation
Fox [2004]	0.73	3.5	1-D	Exobase approximation
This study	0.28	1.62	3-D	DSMC
			Dissociative Recombination of CO^+	
Fox and Hać [1999][c]	0.019	0.58	1-D	Monte Carlo
Nagy et al. [2001][e]	0.27[e]	3.9[e]	1-D	Two-stream method
Fox and Bakalian [2001]	0.029	0.62	1-D	Exobase approximation
Fox [2004]	0.128	0.77	1-D	Exobase approximation
Cipriani et al. [2007][b]	0.00025	0.023	1-D[d]	Monte Carlo test particle
This study	0.058	0.26	3-D	DSMC

[a]Fluxes are in $10^6\ cm^{-2}\ s^{-1}$.
[b]Global escape rates are converted to global averaged escape fluxes at the altitude of 400 km.
[c]Eroded case.
[d]Kim atmosphere [*Kim et al.*, 1998].
[e]*Nagy et al.* [2001] included photodissociation of CO, dissociative recombination of CO^+, and collisions with hot O in their computation. They provided the combined global averaged escape rate and flux for all photochemical mechanisms.

Table 2. Escape Rates of Hot C for Different Source Mechanisms for Different Seasons and Solar Cycle

10^{23} s^{-1}	Aphelion (A)		Equinox (E)		Perihelion (P)	
Solar Activity	Low (L)	High (H)	Low (L)	High (H)	Low (L)	High (H)
Photodissociation of CO (PD)	4.02	-	4.94	29.4	8.42	46.6
Dissociative recombination of CO^+ (DR)	1.26	-	1.05	4.76	1.31	8.54
Sputtering[a]	-	-	1.5	-	-	-
Sputtering[b]	-	-	1.8, 0.5	-	-	-
Sputtering[c]	-	-	0.09,0.0004,2	-	-	-
Ion escape[d]	-	-	$\leq$30	$\leq$232	-	-

[a]Originally calculated by *Luhmann et al*. [1992] and corrected by *Jakosky et al*. [1994]. Sputtering rate of CO_2 (molecules/s).
[b]Sputtering of CO_2 and CO in the "atmosphere of multispecies atom-like molecules" at 1 EUV calculated by *Leblanc and Johnson* [2002].
[c]Quiet solar activity case. Escape rates of CO_2, CO, and C are estimated by *Wang et al*. [2014].
[d]Upper limits to the C-containing ion escape estimated by *Fox* [1997b].

Nagy et al. [2001] used a two-stream calculation adopting the ionosphere description from *Fox and Hać* [1999] and *Kim et al*. [1998]. The differences between those two models are inherent in the slightly different descriptions of the background atmosphere and the local parameters (e.g., collisional cross section), where the main discrepancy comes from the different numerical schemes. *Fox* [2004] included dissociative recombination of CO_2^+ together with other minor mechanisms to study the sources of ambient and escaping C atoms. They predicted that the most important source mechanism is photodissociation of CO, followed by electron impact dissociation of CO as the second most important mechanisms rather than dissociative recombination of CO^+. *Cipriani et al*. [2007] used a 1-D spherical Monte Carlo test particle approach to investigate the production of hot molecules (CO_2 and CO) in addition to hot O and C atoms. Their estimated escape rates C from dissociative recombination of CO^+ for both low and high solar activity are more than an order of magnitude lower than other model results, including the current study results. Furthermore, *Cipriani et al*. [2007] have adopted the universal potential in their molecular dynamic scheme to describe collisions with ambient atmosphere and stated several drawbacks that affect the energy level relevant to the dissociative recombination process.

Previous models differ from each other by ranges of different factors including different numerical schemes and descriptions of background atmosphere and interaction between the nascent and ambient species. According to Table 1, the previous models have employed one-dimensional thermosphere/ionosphere atmosphere describing the background atmosphere spherically symmetric on the dayside. The simulations with a one-dimensional background atmosphere essentially neglect the pure three-dimensional effects, which account for spatial variation of densities and fluxes due to nonaxisymmetry of the thermospheric/ionospheric structure, horizontal velocity of particles, zonal/meridional winds, and planetary rotation. Moreover, the 3-D thermosphere and ionosphere accounts for the spatial variation of collisional frequency between a nascent hot C and a background cold atmospheric species, which depends on the spatial distribution of background atmosphere densities (explained in detail in section 4). The global escape fluxes from each source mechanism for low/high solar activity from this study are higher/lower than those calculated by *Fox and Hać* [1999], *Nagy et al*. [2001], and *Fox and Bakalian* [2001], whereas the results from *Fox* [2004] and *Cipriani et al*. [2007] are the upper and lower limits to the current estimation of the global C escape, respectively.

Table 2 shows our estimated global escape rates for different solar conditions and seasons. The escape rates are computed separately for the two source mechanisms included in this paper and compared with those from sputtering and ion escape. Our escape rates for the two extreme cases at the AL and PH cases range from 4.02×10^{23} s^{-1} to 46.6×10^{23} s^{-1} for photodissociation of CO and from 1.26×10^{23} s^{-1} to 8.54×10^{23} s^{-1} for dissociative recombination of CO^+. The solar cycle variation is a factor of about 5.5–6 and 4.5–6.5 for the former and latter reactions, respectively. The variation by seasons is small for the dissociative recombination case, but it is about 1.3–1.6 for photodissociation case, which is similar to the rough estimated ratios of the heliocentric distances, $(1.5/1.38)^2 \sim 1.18$ and $(1.67/1.5)^2 \sim 1.24$. Our escape rate from dissociative recombination of CO^+ for the AL case is slightly larger than that for the EL case. As shown in Figures 5a and 5b, hot spots of the CO^+ densities are distributed differently for the AL and EL cases. Especially, for the AL case,

there are large hot spots near terminators and south polar regions between altitudes of ~180 km–230 km, inducing slightly larger production of hot C. Since the densities of the thermal species are low at such high altitudes, the larger production rate at AL has a direct impact on the escape of hot C and results in a larger escape rate for AL. Overall, the total escape rate we estimate ranges ~ $(5.28–55.1) \times 10^{23}$ s^{-1} for the aphelion solar low to perihelion solar high case.

As shown in Table 2, the global sputtering loss rate of CO_2 computed by *Luhmann et al*. [1992] for low solar activity is about 1.5×10^{23} s^{-1} (a factor of ~2 numerical error was corrected by *Jakosky et al*. [1994]). *Leblanc and Johnson* [2002] estimated the sputtering of CO_2 and CO, which are about 1.8×10^{23} s^{-1} and 5×10^{22} s^{-1}, respectively. The recent calculations by *Wang et al*. [2014] for the quiet Sun case show escape rates of 9×10^{21} s^{-1}, 4×10^{20} s^{-1}, and 2×10^{23} s^{-1} for CO_2, CO, and C, respectively. These C sputtering loss rates (as C, CO, or CO_2) are of the same order of magnitude as our estimated total escape rate from all dominant photochemical source mechanisms for the EL case. If we scale the age of the Sun backward in time and assume that the Sun had been more active, in terms of the ionizing radiations and coronal activity, the solar-induced loss of the primordial Martian atmosphere would be magnified [*Ayres*, 1997]. Previous modeling studies for the earlier history of the Martian atmosphere [e.g., *Luhmann et al*., 1992; *Zhang et al*., 1993] have suggested that nonthermal escape of C due to photochemistry and exospheric erosion of hot C corona by the solar wind may have played significant roles in CO_2 loss in the content of the early Martian atmosphere. The escape rate of C induced by photodissociation of CO and dissociative recombination of CO^+ is assumed to be enhanced in the past due to the larger photoionization rate of about 5 times contemporary value (i.e., larger electron and CO^+ densities) [*Ayres*, 1997] and the increase of the fraction of CO in the thermosphere [*Fox and Hać*, 1999]. The sputtering of C is expected to be more efficient and likely to be orders of magnitudes larger in the earlier Martian history than the values at present.

5. Conclusion

In this study, our 3-D kinetic particle model with the Mars exospheric code, Mars-AMPS, is coupled with the 3-D MTGCM thermosphere/ionosphere model as described in Paper I to simulate the Martian hot C corona. A self-consistent global description of the Martian upper thermosphere and exosphere is provided for studying the variations associated with different solar activities and seasons in the hot C corona from a local to global perspective. The source reactions that we have considered are the major ones found by *Fox and Bakalian* [2001] and *Fox and Hać* [1999], namely, photodissociation of CO and dissociative recombination of CO^+. *Fox* [2004] also suggested electron impact dissociation of CO as the second most important source of escaping hot C, following photodissociation of CO. While the main sources of hot C are not firmly agreed upon, this work assumed that photodissociation of CO and dissociative recombination of CO^+ are the two major sources of hot C in the Martian thermosphere. This assumption is based on the majority of the previous studies [*Cipriani et al*., 2007; *Fox and Bakalian*, 2001; *Fox and Hać*, 1999; *Nagy et al*., 2001].

The solar cycle and seasonal variations of background temperatures and global winds affect not only the magnitudes of the local parameters such as $V_{threshold}$ but also the spatial distributions of the parent molecule and ion of the source reactions. Depending on the mass of the species, the spatial distributions of the neutral species in this study show different patterns depending on the background temperatures or winds. These different responses by the thermosphere/ionosphere allow the implementation of realistic features such as the winter polar warming. The different local thermalization rates due to variations in the local collisional frequencies result in the reasonable hot C distributions and escape fluxes for the cases considered. The variations in the lower atmosphere are likely to have greater impacts on the CO density than the CO^+ density. This implies that CO mixing ratios will likely be affected during dust storm events (at a constant altitude), having corresponding impacts on the production of hot C as a function of altitude. The bulges of hot C shown in the resulting hot C density distribution maps indicate the locations of hot C with relatively high concentrations in the exosphere. These locations change annually due to the seasonal effects, providing an implication of high hot C density detections in the possible measurements.

The overall characteristics in the variations of the hot C distributions and the escape rates are likely reasonably calculated here. For a more realistic description for collisions of hot C with the ambient neutral species, our model will implement any new improvement in the collision scheme and cross section. It has been suggested that such is the case in hot O calculation when including hot O and thermal O collisions

usingthe angular dependence of the differential collision cross section of *Kharchenko et al*. [2000]; however, such basic information for hot C collisions is not available.

Our computed global escape rates of hot C atoms range from about $5.28 \times 10^{23}\ s^{-1}$ for the aphelion solar low activity case to about $55.1 \times 10^{23}\ s^{-1}$ for the perihelion solar high activity case. We have compared our hot C escape rates with those calculated by other previous models. However, the discrepancies between models are difficult to identify because of numerous different factors, including different numerical schemes and the descriptions of the background atmosphere and the interaction between nascent and ambient species. At present epoch, nonthermal mechanisms play a dominant role in the loss of C from the Martian atmosphere. However, modeling studies of the ancient Martian atmosphere [e.g., *Luhmann et al*., 1992; *Zhang et al*., 1993] suggested that more vulnerability to sputtering than to other escape mechanisms is expected at earlier epochs. We expect to expand our knowledge about these loss processes at the Martian atmosphere by the in situ measurement of the upper atmosphere from the Mars Atmosphere and Volatile EvolutioN (MAVEN) mission, which will shed light on our investigation of the Martian hot corona.

Acknowledgments

We acknowledge the referees for their thorough reading and constructive suggestions, which helped to improve the first version of this paper. This work has been supported by NASA Mars Fundamental Research Program grant NNX09AL26G. Resources for all simulations in this work have been provided by NASA High-End Computing Capability (HECC) project at NASA Advanced Supercomputing (NAS) Division. Simulation data are available upon request from the author.

References

Ayres, T. (1997), Evolution of the solar ionizing flux, *J. Geophys. Res.*, *102*, 1641–1651, doi:10.1029/96JE03306.

Bell, J. M., S. W. Bougher, and J. R. Murphy (2007), Vertical dust mixing and the interannual variations in the Mars thermosphere, *J. Geophys. Res.*, *112*, E12002, doi:10.1029/2006JE002856.

Berger, M. J., and P. Colella (1989), Local adaptive mesh refinement for shock hydrodynamics, *J. Comput. Phys.*, *82*, 64–84.

Bird, G. A. (1994), *Molecular Gas Dynamics and the Direct Simulation of Gas Flows*, Clarendon Press, Oxford, U. K.

Bougher, S. W., R. G. Roble, E. C. Ridley, and R. E. Dickinson (1990), The Mars thermosphere: 2. General circulation with coupled dynamics and composition, *J. Geophys. Res.*, *95*, 14,811–14,827, doi:10.1029/JB095iB09p14811.

Bougher, S. W., S. Engel, R. G. Roble, and B. Foster (1999), Comparative terrestrial planet thermospheres: 2. Solar cycle variation of global structure and winds at equinox, *J. Geophys. Res.*, *104*, 16,591–16,611, doi:10.1029/1998JE001019.

Bougher, S. W., S. Engel, R. G. Roble, and B. Foster (2000), Comparative terrestrial planet thermospheres. 3. Solar cycle variation of global structure and winds at solstices, *J. Geophys. Res.*, *105*, 17,669–17,692, doi:10.1029/1999JE001232.

Bougher, S. W., R. G. Roble, and T. J. Fuller-Rowell (2002), Simulations of the upper atmospheres of the terrestrial planets, in *Atmospheres in the Solar System: Comparative Aeronomy*, edited by M. Mendillo, A. F. Nagy, and J. H. Waite, AGU, Washington, D. C.

Bougher, S. W., S. Engel, D. P. Hinson, J. R. Murphy (2004), MGS Radio Science electron density profiles: Interannual variability and implications for the neutral atmosphere, *J. Geophys. Res.*, *109*, E03010, doi:10.1029/2003JE002154.

Bougher, S. W., J. M. Bell, J. R. Murphy, M. A. López-Valverde, and P. G. Withers (2006), Polar warming in the Mars thermosphere: Seasonal variations owing to changing insolation and dust distributions, *Geophys. Res. Lett.*, *32*, L02203, doi:10.1029/2005GL024059.

Bougher, S. W., P.-L. Blelly, M. Combi, J. L. Fox, I. Mueller-Wodarg, A. Ridley, and R. G. Roble (2008), Neutral upper atmosphere and ionosphere modeling, *Space Sci. Rev.*, *139*, 107–141, doi:10.1007/s11214-008-9401-9.

Bougher, S. W., T. M. McDunn, K. A. Zoldak, and J. M. Forbes (2009), Solar cycle variability of Mars dayside exospheric temperatures: Model evaluation of underlying thermal balances, *Geophys. Res. Lett.*, *36*, L05201, doi:10.1029/2008GL036376.

Bougher, S. W., D. A. Brain, J. L. Fox, F. Gonzalez-Galindo, C. Simon-Wedlund, and P. G. Wither (2014), Chapter 14: Upper atmosphere and ionosphere, in *Mars Book II*, edited by B. Haberle et al., Cambridge Univ. Press, in press.

Cipriani, F., F. Leblanc, and J. J. Berthelier (2007), Martian corona: Nonthermal sources of hot heavy species, *J. Geophys. Res.*, *112*, E07001, doi:10.1029/2006JE002818.

Curry, S. M., M. Liemohn, X. Fang, Y. Ma, and J. Espley (2013), The influence of production mechanisms on pick-up ion loss at Mars, *J. Geophs, Res. Space Physics*, *118*, 554–569, doi:10.1029/2012JA017665.

Dong, C., S. W. Bougher, Y. Ma, G. Toth, A. F. Nagy, and D. Najib (2014), Solar wind interaction with Mars upper atmosphere: Results from the one-way coupling between the multifluid MHD model and the MTGCM model, *Geophys. Res. Lett.*, *41*, 2708–2715, doi:10.1002/2014GL059515.

Fang, X., M. W. Liemohn, A. F. Nagy, Y. Ma, D. L. De Zeeuw, J. U. Kozyra, and T. H. Zurbuchen (2008), Pickup oxygen ion velocity space and spatial distribution around Mars, *J. Geophys. Res.*, *113*, A02210, doi:10.1029/2007JA012736.

Fang, X., S. W. Bougher, R. E. Johnson, J. G. Luhmann, Y. Ma, Y.-C. Wang, and M. W. Liemohn (2013), The importance of pickup oxygen ion precipitation to the Mars upper atmosphere under extreme solar wind conditions, *Geophys. Res. Lett.*, *40*, 1922–1927, doi:10.1002/grl.50415.

Forget, F., F. Montmessin, J.-L. Bertaux, F. González-Galindo, S. Lebonnois, E. Quémerais, A. Reberac, E. Dimarells, and M. A. López-Valverde (2009), Density and temperatures of the upper Martian atmosphere measured by stellar occultation with Mars Express SPICAM, *J. Geophys. Res.*, *114*, E01004, doi:10.1029/2008JE003086.

Fox, J. L. (1997a), Spectrum of hot O at the exobases of the terrestrial planets, *J. Geophys. Res.*, *102*, 24,005–24,011, doi:10.1029/97JA02089.

Fox, J. L. (1997b), Upper limits to the outflow of ions at Mars: Implications for atmospheric evolution, *Geophys. Res. Lett.*, *24*, 2901–2904, doi:10.1029/97GL52842.

Fox, J. L. (2004), CO_2^+ dissociative recombination: A source of thermal and nonthermal C on Mars, *J. Geophys. Res.*, *109*, A08306, doi:10.1029/2004JA010514.

Fox, J. L., and A. B. Hać (1999), Velocity distributions of C atoms in CO^+ dissociative recombination: Implications for photochemical escape of C from Mars, *J. Geophys. Res.*, *104*, 24,729–24,737, doi:10.1029/1999JA900330.

Fox, J. L., and A. B. Hać (2009), Photochemical escape of oxygen from Mars: A comparison of the exobase approximation to a Monte Carlo method, *Icarus*, *204*, 527–544, doi:10.1016/j.icarus.2009.07.005.

Fox, J. L., and F. M. Bakalian (2001), Photochemical escape of atomic carbon from Mars, *J. Geophys. Res.*, *106*, 28,785–28,795, doi:10.1029/2001JA000108.

Fox, J. L., and J. H. Black (1989), Photodissociation of CO in the thermosphere of Venus, *Geophys. Res. Lett.*, *16*, 291–294, doi:10.1029/GL016i004p00291.

Fox, J. L., and K. Y. Sung (2001), Solar activity variations of the Venus thermosphere/ionosphere, *J. Geophys. Res.*, *106*, 21,305–21,335, doi:10.1029/2001JA000069.

Haberle, R. M., M. M. Joshi, J. R. Murphy, J. R. Barnes, J. T. Schofield, G. Wilson, M. Lopez-Valverde, J. L. Hollingsworth, A. F. C. Bridger, and J. Schaeffer (1999), General circulation model simulations of the Mars Pathfinder atmospheric structure investigation/meteorology data, *J. Geophys. Res.*, *104*, 8957–8974, doi:10.1029/1998JE900040.

Hodges, R. R. (2000), Distributions of hot oxygen for Venus and Mars, *J. Geophys. Res.*, *105*, 6971–6981, doi:10.1029/1999JE001138.

Ip, W.-H. (1988), On a hot oxygen corona of Mars, *Icarus*, *76*, 135–145.

Jakosky, B. M., R. O. Pepin, R. E. Johnson, and J. L. Fox (1994), Mars atmospheric loss and isotropic fractionation by solar-wind-induced sputtering and photochemical escape, *Icarus*, *111*, 271–288.

Johnson, R. E. (1994), Plasma-induced sputtering of an atmosphere, *Space Sci. Rev.*, *69*, 215–253.

Kharchenko, V., A. Dalgarno, B. Zygelman, and J.-H. Yee (2000), Energy transfer in collisions of oxygen atoms in the terrestrial atmosphere, *J. Geophys. Res.*, *105*(A11), 24,899–24,906, doi:10.1029/2000JA000085.

Kim, J., A. F. Nagy, J. L. Fox, and T. E. Cravens (1998), Solar cycle variability of hot oxygen atoms at Mars, *J. Geophys. Res.*, *103*, 29,339–29,342, doi:10.1029/98JA02727.

Lammer, H., and S. J. Bauer (1991), Nonthermal atmospheric escape from Mars and Titan, *J. Geophys. Res.*, *96*(A2), 1819–1825, doi:10.1029/90JA01676.

Leblanc, F., and R. E. Johnson (2001), Sputtering of the Martian atmosphere by solar wind pick-up ions, *Planet. Space Sci.*, *49*, 645–656.

Leblanc, F., and R. E. Johnson (2002), Role of molecular species in pickup ion sputtering of the Martian atmosphere, *J. Geophys. Res.*, *107*(E2), 5010, doi:10.1029/2000JE001473.

Lee, Y., M. R. Combi, V. Tenishev, and S. W. Bougher (2014), Hot carbon corona in Mars' upper thermosphere and exosphere: 1. Mechanisms and structure of the hot corona for low solar activity at equinox, *J. Geophys. Res. Planets*, *119*, 905–924, doi:10.1002/2013JE004552.

Liu, Y., A. F. Nagy, C. P. T. Groth, D. L. DeZeeuw, and T. I. Gombosi (1999), 3D Multi-fluid MHD studies of the solar wind interaction with Mars, *Geophys. Res. Lett.*, *26*, 2689–2692, doi:10.1029/1999GL900584.

Liu, Y., A. F. Nagy, T. I. Gombosi, D. L. DeZeeuw, and K. G. Powell (2001), The solar wind interaction with Mars: Results of three-dimensional three species MHD studies, *Adv. Space Res.*, *27*, 1837–1846.

López-Valverde, M. A., D. T. Edwards, M. López-Puertas, and C. Roldán (1998), Non-local thermodynamic equilibrium in general circulation models of the Martian atmosphere 1. Effects of the local thermodynamic equilibrium approximation on thermal cooling and solar heating, *J. Geophys. Res.*, *103*, 16,799–16,811, doi:10.1029/98JE01601.

Luhmann, J. G., and J. U. Kozyra (1991), Dayside pickup oxygen ion precipitation at Venus and Mars: Spatial distributions, energy deposition, and consequences, *J. Geophys. Res.*, *96*, 5457–5467, doi:10.1029/90JA01753.

Luhmann, J. G., R. E. Johnson, and M. H. G. Zhang (1992), Evolutionary impact of sputtering of the Martian atmosphere by O^+ pickup ions, *Geophys. Res. Lett.*, *19*, 2,151–2,154, doi:10.1029/92GL02485.

Lundin, R., et al. (1990), Aspera/Phobos measurements of the ion outflow from the Martian ionosphere, *Geophys. Res. Lett.*, *17*, 873–876, doi:10.1029/GL017i006p00873.

Ma, Y., and A. F. Nagy (2007), Ion escape fluxes from Mars, *Geophys. Res. Lett.*, *34*, L08201, doi:10.1029/2006GL029208.

Ma, Y., A. F. Nagy, I. V. Sokolov, and K. C. Hansen (2004), Three-dimensional, multispecies, high spatial resolution MHD studies of the solar wind interaction with Mars, *J. Geophys. Res.*, *109*, D15515, doi:10.1029/2003JA0010367.

McElroy, M. B., T. Y. Kong, and Y. L. Yung (1977), Photochemistry and evolution of Mars' atmosphere: A Viking perspective, *J. Geophys. Res.*, *82*(28), 4379–4388, doi:10.1029/JS082i028p04379.

Nagy, A. F., M. W. Liemohn, J. L. Fox, and J. Kim (2001), Hot carbon densities in the exosphere of Mars, *J. Geophys. Res.*, *106*, 21,565–21,568, doi:10.1029/2001JA000007.

Paxton, L. J. (1985), Pioneer Venus Orbiter ultraviolet spectrometer limb observations: Analysis and interpretation of the 166- and 156-nm data, *J. Geophys. Res.*, *90*, 5089–5096, doi:10.1029/JA090iA06p05089.

Tenishev, V., M. R. Combi, and B. Davidsson (2008), A global kinetic model for cometary comae. The evolution of the coma of the Rosetta target comet Churyumov-Gerasimenko throughout the mission, *Astrophys. J.*, *685*, 659–677.

Tenishev, V., M. Rubin, O. J. Tucker, M. R. Combi, and M. Sarantos (2013), Kinetic modeling of sodium in the lunar exosphere, *Icarus*, *226*, 1538–1549, doi:10.1016/j.icarus.2013.08.021.

Valeille, A., V. Tenishev, S. W. Bougher, M. R. Combi, and A. F. Nagy (2009a), Three-dimensional study of Mars upper thermosphere/ionosphere and hot oxygen corona: 1. General description and results at equinox for solar low conditions, *J. Geophys. Res.*, *114*, E11005, doi:10.1029/2009JE003388.

Valeille, A., M. R. Combi, S. W. Bougher, V. Tenishev, and A. F. Nagy (2009b), Three-dimensional study of Mars upper thermosphere/ionosphere and hot oxygen corona: 2. Solar cycle, seasonal variations, and evolution over history, *J. Geophys. Res.*, *114*, E11006, doi:10.1029/2009JE003389.

Valeille, A., M. R. Combi, V. Tenishev, S. W. Bougher, and A. F. Nagy (2010a), A study of suprathermal oxygen atoms in Mars upper thermosphere and exosphere over the range of limiting conditions, *Icarus*, *206*, 18–27, doi:10.1016/j.icarus.2008.08.018.

Valeille, A., M. R. Combi, V. Tenishev, S. W. Bougher, and A. F. Nagy (2010b), Water loss and evolution of the upper atmosphere and exosphere over Martian history, *Icarus*, *206*, 28–39, doi:10.1016/j.icarus.2009.04.036.

Verigin, M. I., et al. (1991), Ions of planetary origin in the Martian magnetosphere (PHOBOS 2/TAUS experiment), *Planet. Space Sci.*, *39*, 131–137.

Wang, Y. C., J. G. Luhmann, F. Leblanc, X. Fang, R. E. Johnson, Y. Ma, W.-H. Ip, and L. Li (2014), Modeling of the O^+ pickup ion sputtering efficiency dependence on solar wind conditions for the Martian atmosphere, *J. Geophys. Res. Planets*, *119*, 93–108, doi:10.1002/2013JE004413.

Yagi, M., F. Leblanc, J. Y. Chaufray, F. Gonzalez-Galindo, S. Hess, and R. Modolo (2012), Mars exospheric thermal and non-thermal components: Seasonal and local variations, *Icarus*, *221*, 682–693.

Zhang, M. H. G., J. G. Luhmann, S. W. Bougher, and A. F. Nagy (1993), The ancient oxygen exosphere of Mars—Implications for atmosphere evolution, *J. Geophys. Res.*, *98*(17), 10,915–10,923, doi:10.1029/93JE00231.